8-2022

The structure of 71Ni via beta-delayed neutron spectroscopy of 71Co

Andrew Keeler
University of Tennessee, Knoxville, akeeler@vols.utk.edu

To the Graduate Council:

I am submitting herewith a dissertation written by Andrew Keeler entitled "The structure of 71Ni via beta-delayed neutron spectroscopy of 71Co." I have examined the final electronic copy of this dissertation for form and content and recommend that it be accepted in partial fulfillment of the requirements for the degree of Doctor of Philosophy, with a major in Physics.

Robert Grzywacz, Major Professor

We have read this dissertation and recommend its acceptance:

Miguel Madurga-Flores, Nadia Fomin, Lawrence Heilbronn

Accepted for the Council:

Dixie L. Thompson

Vice Provost and Dean of the Graduate School

(Original signatures are on file with official student records.)

The structure of 71Ni via beta-delayed neutron spectroscopy of 71Co

A Dissertation Presented for the

Doctor of Philosophy

Degree

University of Tennessee, Knoxville

Andrew Keeler

August 2022

For my grandfather, whose desire to understand the physical world spurred my own.

Abstract

Studies of beta decays can give insights into the underlying structure of the nucleus. In particular, decays of closed-shell and near-closed-shell nuclei can provide important benchmarks for structure models, which are used in simulations of r-process nucleosynthesis. This work reports on a study of beta decays of ^{71}Co produced in an experiment that was carried out in October 2016 at MSU's National Superconducting Cyclotron Laboratory (NSCL) using the Versatile Array of Neutron Detectors at Low Energy (VANDLE). In order to carry out this experiment, a novel position-sensitive scintillating detector was developed to enable the sub-nanosecond timing response that VANDLE requires, which traditional silicon-based position-sensitive detectors would be unable to provide. This experiment marked the first time that VANDLE was used in a decay spectroscopy experiment at a fragmentation facility.

The beta decay strength distribution for ^{71}Co beta decay is determined above the neutron separation energy in ^{71}Ni, and direct measurement of the beta-delayed neutron branching ratio is reported. The neutron branching ratio is higher than found in past measurements that sought to estimate it by measuring gamma-ray coincidences. Shell model calculations can explain the experimental data only when an effective Z=28 Shell gap is less than 2 MeV in ^{71}Ni, a significant reduction over the 5 MeV expected near ^{78}Ni.

Table of Contents

List of Figures

Chapter 1: Introduction

1.1 Nuclear Structure near Doubly Magic ^{78}Ni

The evolution of the magic numbers far from stability remains a topic of interest due to the implications on nuclear structure models. Currently, structure models that are accurate near stability do not reliably extend to far-from-stability regions of the nuclear chart, so measurements in the far-from-stability regions, particularly of simple magic nuclei, are essential for constraining those models (Erler et al., 2012; Huck et al., 1985; Madurga et al., 2012; Mazzocchi et al., 2013; Taniuchi et al., 2019; Wienholtz et al., 2013). Such structure models are essential for understanding and modeling behavior of very neutron-rich nuclei that cannot be measured directly, particularly those that lie along the r-process path (see **section 1.2**). ^{78}Ni and the nuclei surrounding it comprise a key region for understanding the evolution of the both the Z=28 and N=50 magic numbers far from stability.

An important tool which can be used to make predictions for the observables of nuclear behavior are nuclear structure models, one of the most widely used of which is the nuclear shell model. The nuclear shell model makes predictions about nuclear behavior by modeling the nucleons as moving in a three-dimensional, finite potential well. This leads to the emergence of discrete nucleon orbitals which are progressively filled since nucleons, being fermions, obey the Pauli Exclusion principle. The addition of spin-orbit terms (Mayer, 1949) leads to gaps in the nucleon orbitals that correspond to the magic numbers, which suggests that the magic numbers may be modified if the energies of the various orbitals change relative to each other. A fuller look at the fundamentals of the nuclear shell model is presented in **section 2.2**.

When performing shell-model calculations, a distinction is made between tightly-bound "core" nucleons and the valence nucleons that occupy the higher-energy orbitals. Calculations generally treat the core nucleons as inert, since any excitation of these tightly-bound nucleons would necessarily involve significant amounts of energy, and so would likely be disfavored relative to excitations of valence nucleons for which the energies involved would be much smaller. This allows for the calculation of energy levels of heavy nuclei, for which the model

space would otherwise be intractable due to the large number of nucleons. Shell model codes such as NushellX, Antoine, or Kshell (Caurier, 2004; Rae, 2008; Shimizu, 2013), are popularly used to perform these computations. They typically use realistic effective interactions derived from free nucleon-nucleon forces that are converted to in-medium forces using effective field theory methods (Hjorth-Jensen et al., 1995).

The nuclear shell model is highly successful at modeling nuclei near magic numbers. For example, along the Z=28 magic number shell model calculations predict the existence of a long-lived 8+ excited state in even-even nuclei as a consequence of the closed proton shell. Such an isomer state is observed in ^{70}Ni (Sawicka et al., 2004) and ^{76}Ni (Söderström & et al., 2015), however, observations of ^{72}Ni and ^{74}Ni (Sawicka et al., 2004) notably failed to find evidence of the state. Studies since have offered several explanations for the non-observation (Lisetskiy et al., 2004; Van Isacker, 2011) and attempts to locate the state (Mazzocchi et al., 2005; Morales & et al., 2016; Rajabali et al., 2012), but with at best inconsistent results. The current leading explanation suggests that a deformed shell structure would create a fast de-excitation pathway for the state, causing the state to present as a short-lived, gamma-emitting state instead of an isomer, but the question remains open.

An alternative test of magicity in this region is to measure the size of the shell gap by observing its effects on the beta decay characteristics of the magic nuclei. The effect of spin-orbit splitting on the 0f orbital causes a shell gap to appear between the $0f_{7/2}$ orbital and the $0f_{5/2}$ orbital, with the $f_{7/2}$ orbital making up the shell between the magic numbers 20 and 28, with the $f_{5/2}$ orbital clustering together with the $p_{1/2}$, $p_{3/2}$, and $g_{9/2}$ orbitals to form the shell between magic numbers 28 and 50. The fact that the spin-orbit-partner f-orbitals occupy these different shells leads to a signature beta decay characteristic: decays of neutron-rich cobalt isotopes, for which there is a single opening in the $f_{7/2}$ proton orbital, will be dominated by transitions that populate that opening via the decay of a neutron from the $f_{5/2}$ neutron orbital. Decays of neutrons from the p- and g- orbitals are blocked from directly populating the $f_{7/2}$ orbital by spin-orbit considerations, and so would instead populate p- and g- proton orbitals, above the Z=28 shell gap. Measuring the energy difference between these sets of transitions gives a direct measure of the size of the Z=28 shell gap (Figure 1).

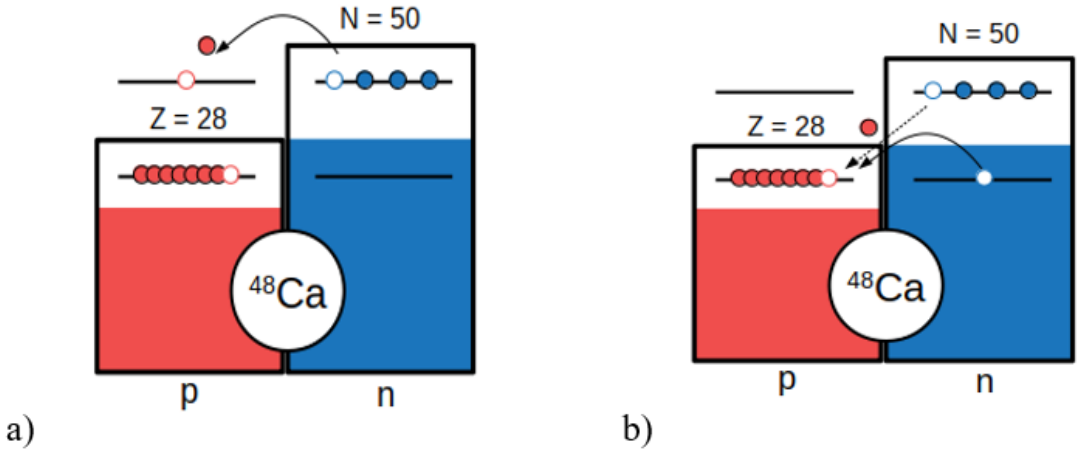

Figure 1: Cartoon of neutron-rich Co decay assuming a ^{48}Ca core. a) Decays of the valence $f_{5/2}$ neutrons to the $f_{7/2}$ are allowed GT transitions (dashed line) while decays of $g_{9/2}$ and p-orbital neutrons would be blocked from directly populating the $f_{7/2}$ proton hole. Decays of core $f_{7/2}$ neutrons are also allowed but are energetically unfavorable (solid line). b) Valence $g_{9/2}$ and p-orbital neutrons can populate proton g- and p- orbitals above the Z=28 proton shell gap in allowed decays. The excitation energies of these resulting states are all translated up relative to the $f_{5/2} \rightarrow f_{7/2}$ transition by the size of the shell gap.

Recent work by (Spyrou et al., 2016) used Total Absorption Spectroscopy (TAS) to make this measurement for ^{70}Co. That experiment suggested a significantly reduced Z=28 shell gap in ^{70}Ni and observed a surprising amount of high-excitation transition intensity, which resulted in their shell model calculations unexpectedly under-predicting their data by a significant margin. Generally shell model calculations systematically over-predict the transition intensities they model and need to be quenched to reach agreement with experimental data, so shell model calculations under-predicting data is quite notable. A similar TAS measurement was carried out on beta decays of ^{71}Co by (Lyons et al., 2019). Lyons provided a map of beta decay transition intensity up to the neutron separation energy in ^{71}Ni but could only provide a lower bound on the transition intensities to states above the neutron separation energy.

This work would extend the map of those intensities in the decays of ^{71}Co above the neutron separation energy to provide a complete picture of the beta decay transitions, allowing for more complete comparisons to shell model predictions. This will give additional data for modeling potential modifications to the Z=28 shell and serve as a means to perform similar analysis on decays of ^{72}Co, for which TAS data does not yet exist. Additionally, this work will perform a direct measurement of the beta-delayed neutron emission branching ratio for ^{71}Co, for which there is a curious inconsistency in the available literature. (Mazzocchi et al., 2005) claims to establish a lower limit for this value of 3%, (Rajabali et al., 2012) later claims to establish an upper limit of 2.7%. A direct measurement of this value would help resolve this inconsistency.

1.2 R-Process Nucleosynthesis

The rapid neutron capture process (r-process) is an astrophysical nucleosynthesis process that is generally believed to occur in neutron star mergers and supernovae (Burbidge et al., 1957). In the r-process, repeated neutron captures followed by beta decays of stellar nuclei allow for the creation of elements heavier than ^{56}Fe, which are not energetically favorable in fusion reactions due to their lower binding energy. Due to the high neutron flux in r-process sites, the neutron capture processes occur much more rapidly than beta decays, pushing the r-process pathway to the extremely neutron-rich region, far from stability. Eventually an equilibrium is reached between the neutron capture reaction (n,γ) and the reverse, photodisintegration reaction

(γ,n), allowing enough time for the slower beta decay processes to occur. Several of these equilibrium points occur when the nuclei involved reach a magic number corresponding to a closed neutron shell, sometimes called "waiting point nuclei," where the addition of another neutron corresponds to a very low neutron separation energy and thus a greatly increased photodisintegration rate. In some environments waiting point nuclei are reached when the neutron capture rate equilibrates directly with the beta decay rate. Once the neutron flux drops and the nuclei decay back to stability, the final abundance pattern shows clear peaks corresponding to these waiting points.

Studies of the r-process involve modeling with complex reaction networks due to the number of nuclei involved in the reactions and decay processes. These simulations require detailed nuclear structure inputs, particularly neutron capture cross sections, beta decay half-lives, and delayed-neutron branching ratios of the involved nuclei. Since the main path lies so far from stability and involves many unknown nuclei that are inaccessible to current experimental efforts, the use of nuclear structure models is required to estimate the reaction and decay behavior of these nuclei. As discussed previously, near-stability structure models only inconsistently extend into the very neutron-rich region, so benchmarks of simple, closed-shell nuclei like ^{78}Ni provide essential inputs for constraining these structure models. (Mumpower et al., 2016)

Chapter 2: Theoretical Basis

2.1 Beta Decay

Unstable beta-decaying nuclei will decay back toward the so-called valley of stability. In the case of beta decay modes, the nuclei seek a more energetically favorable distribution of protons and neutrons by the conversion of one into the other. The two most prevalent modes are β- and β+ decays, though others exist as well, including electron capture and various double-decay modes. In β- decay, a neutron converts into a proton via the emission of an electron and an antineutrino, while β+ decays convert a proton into a neutron via the emission of a positron and a neutrino (β+ decay). In both these processes, the total number of nucleons remains unchanged.

$$\beta\text{-}: {}^{A}_{Z}X_N \rightarrow {}_{Z+1}{}^{A}X_{N-1} + e^- + \bar{\nu}_e$$
$$\beta\text{+}: {}^{A}_{Z}X_N \rightarrow {}_{Z-1}{}^{A}X_{N+1} + e^+ + \nu_e$$

β+ decays occur predominantly in proton-rich nuclei while β- decays occur in neutron-rich nuclei. The energy available in the decay process ($Q_{\beta\pm}$) is given by the difference in ground-state masses of the parent and daughter nuclei. This energy in the β- (β+) decay is shared between the daughter nucleus and the emitted electron (positron) and antineutrino (neutrino). A beta decay mode is energetically favorable if the corresponding Q-value is positive, and energetically unfavorable if that Q-value is negative. For the remainder of this work, Q_β will refer to the β- form.

$$\beta\text{-}: Q_{\beta-} = [M({}^{A}_{Z}X_N) - M({}_{Z+1}{}^{A}X_{N-1})]c^2$$
$$\beta\text{+}: Q_{\beta+} = [M({}^{A}_{Z}X_N) - M({}_{Z-1}{}^{A}X_{N+1})]c^2$$

The beta decay half-life is given by the following equation (Krane & Lynch, 1989):

$$T_{1/2}^{-1} = \sum_{E_i \geq 0}^{E_i \leq Q_\beta} S_\beta(E_i) \times f\left(Z,\, Q_\beta - E_i\right) \qquad [1]$$

Here, S_β, which is called the strength function, is the matrix element of the transition operator for the decay of the parent nucleus to the energy state E_i in the daughter and f is the Fermi integral, a factor that reflects the amount of phase space available to the transition due to the 3-body nature of the decay. The Fermi integral, which scales as $(Q_\beta - E_i)^5$, has the effect of amplifying the observed intensity of transitions to low-lying daughter states and suppressing the transitions to higher-energy states (Figure 2). Since the Fermi integral contains only information on the energetics of the decay and no structure information, discussions of structure will often decompose equation [1] into a series of partial half-lives for each transition element in S_β. and divide each transition by the corresponding Fermi integral, isolating the structure information of the nucleus on the right side of the equation.

$$ft_i = S_\beta(E_i)^{-1} \text{ where } T_{1/2}^{-1} = \sum_i t_i^{-1}$$

In practice, these *ft*-values can span many orders of magnitude, so it is more common to see references to the $\log_{10}ft$, referred to as the comparative partial half-life for the transition.

2.1.1 Allowed decays

Allowed decays are beta decays in which the orbital angular momentum of the nucleus does not change. In Fermi-type allowed decays, the electron and neutrino are emitted in an angular momentum singlet state ($J = 0$), which constrains transitions to between nucleon orbitals with the same angular momentum quantum numbers.

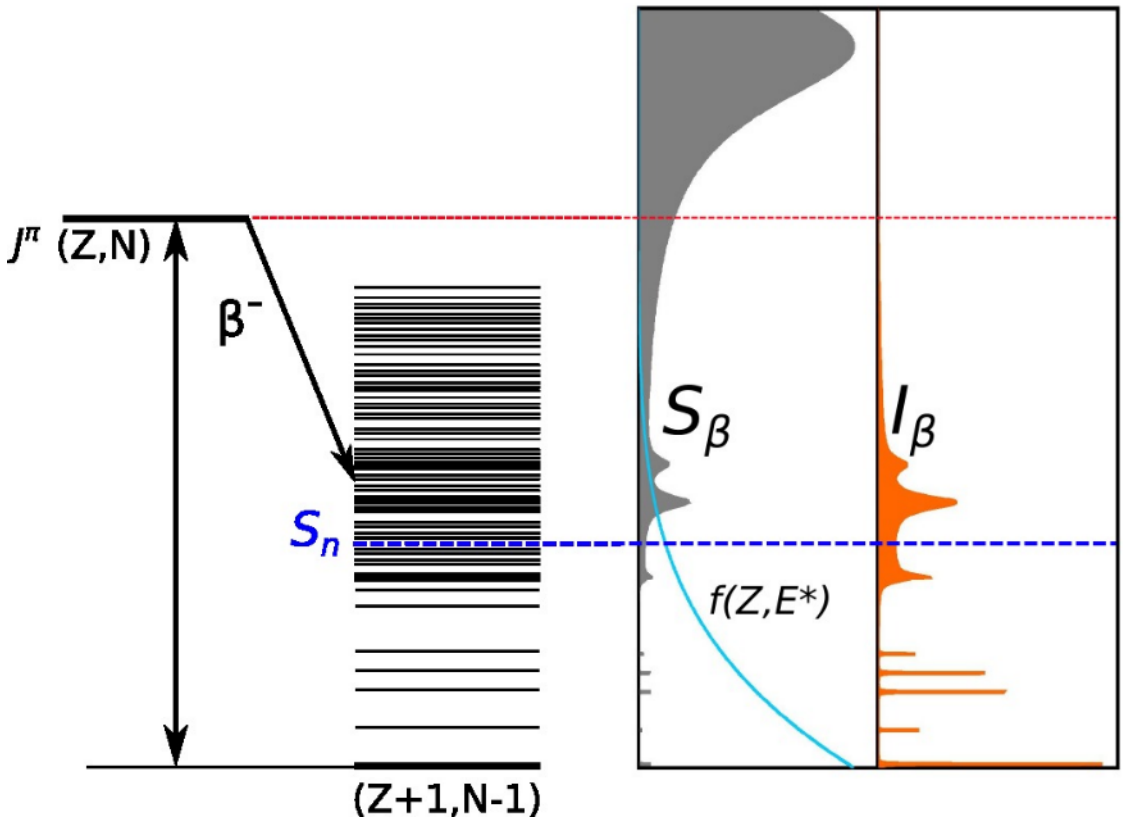

Figure 2: Beta decay scheme. The level density in the daughter nucleus is described by S_β, while the observed branching ratios (I_β) are given by folding S_β with the Fermi integral. Decays to states above S_n may lead to the emission of delayed neutrons.

The Fermi decay operator is written as:

$$\sum_{i=0}^{A} \tau^{\pm}(i)$$

where $\tau^{\pm}$ are the isospin ladder operators.

In Gamow-Teller-type (GT) decays, the electron and neutrino are emitted in the triplet state ($J = 1$) which allows for nucleon transitions between spin-orbit partner states with different total angular momentum ($\Delta J = 0, \pm 1$). The Gamow-Teller decay operator is written as:

$$\sum_{i=0}^{A} \sigma(i)\tau^{\pm}(i)$$

where σ is the Pauli spin operator and $\tau^{\pm}$ are the isospin ladder operators, as in the case of Fermi decays. Since the orbital angular momentum (l) remains unchanged, Gamow-Teller decays are sometimes referred to as "spin-flip, isospin flip" decays, reflecting the influence of the spin operator on the transition and the total angular momentum.

2.1.2 Forbidden Decays

Forbidden decays are beta decays in which the emitted electron and antineutrino carry away one or more units of orbital angular momentum from the nucleus, which may result in parity changes between the mother and daughter nuclei, and are termed "forbidden" due to the non-preservation of orbital angular momentum between the initial and final nuclear states. The transition operator describing these transitions includes successive powers of $\frac{i\bar{p}\cdot\bar{r}}{\hbar}$, representing the angular momentum contribution to the transition amplitude. The addition of various powers of momentum terms to the transition operators results in a heavy suppression of the probability for these kinds of decays to occur relative to allowed decays. First forbidden decays (those for which the transition operator contains a first power of $\frac{i\bar{p}\cdot\bar{r}}{\hbar}$, and for which $\Delta l = \pm 1$) are the most common of these kinds of decays. Each successive degree of forbiddenness results in a greater change in orbital angular momentum and an increase in the *ft* for the transition by about 4 orders

of magnitude relative to the previous degree of forbiddenness since the momentum contribution to the transition probability is on the order 10^{-4}.

2.1.3 Beta-delayed Neutron Emission

As nuclei become more neutron rich, Q_β increases. Simultaneously, the neutron separation energy (S_n) decreases, eventually falling below Q_β for very neutron-rich nuclei. For decays in which the neutron separation energy of the daughter nucleus is smaller than the Q_β value for the beta decay, beta decays may end up populating neutron-unbound states in the daughter nucleus, resulting in the possibility of a beta-delayed neutron emission (Figure 3).

First discovered in 1939 by (Roberts et al., 1939) delayed neutron emission as a phenomenon occupies an important position in low-energy nuclear physics. Many fission fragments are delayed neutron emitters, so the neutrons emitted by these fragments play a significant role in the free neutron abundance and resulting decay heat in nuclear reactors. Additionally, delayed neutron emission provides a competing de-excitation pathway for daughter nuclei to gamma-ray de-excitation following beta decay. Studies that attempt to use gamma-ray spectroscopy to construct S_β functions for nuclei of interest will be insensitive to neutron-emission pathways populating the ground state of the emission daughter, and so are likely to incorrectly assign strength from above S_n to lower-lying states. Neutron spectroscopy is needed to accurately reconstruct S_β above S_n in very neutron-rich regions due to the significant probability of these neutron-emitting decay branches.

2.2 Nuclear Shell Model

Bound nucleons, being fermions, occupy distinct energy levels in a central potential in accordance with the Pauli exclusion principle. Unlike the analogous atomic shells occupied by the electrons, for which the electric charge of the nucleus provides a central potential, the central potential for the nucleons themselves is an effective one due to the interactions of the nucleons themselves. Nucleons are described as being in one of several “shells” that are made up of

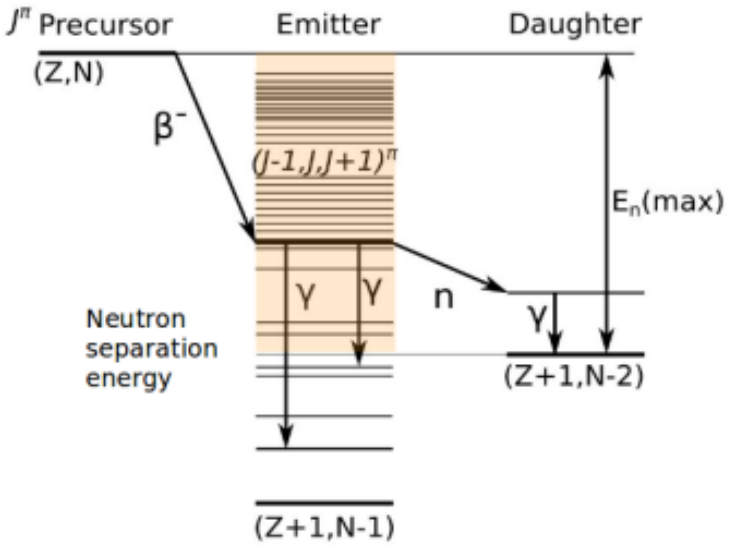

Figure 3: Decay scheme for beta-delayed neutron emission. Beta transitions populating excited states above S_n in the emitter nucleus may de-excited via neutron emission instead of gamma emission. The energy of the emitted neutron will be equal to the energy of the emitter state minus S_n and any excitation energy remaining in the resulting daughter nucleus, which would be observed as coincident gamma rays.

energetically close-lying orbitals, with notable gaps between shells where the spacing between orbitals becomes larger. These gaps are caused by splittings of the orbitals due to energy, angular momentum, and spin-orbit effects, and give rise to the so-called "magic numbers" of nucleons. These "magic" closed-shell nuclei are marked by discontinuities in beta decay Q-values and increased energy requirements to add additional nucleons to the nucleus, corresponding to the energy gap between the filled nucleon shell and the next open one (Figure 4).

Since protons and neutrons occupy their own distinct orbitals, a nucleus may have either a magic number of protons or neutrons, or both. Such "doubly magic" nuclei are important benchmarks for structure models due to their relatively simple structural characters. Of particular note are the doubly magic nuclei that are highly proton- or neutron-rich, such as ^{100}Sn or ^{78}Ni. Such exotic doubly magic nuclei provide important benchmarks for modeling the evolution of shell structure away from the valley of stability, where structure models are much less reliable.

The shell model has significant implications for understanding the systematics of beta decay. The requirement in allowed decays that $\Delta l = 0$ constrains the decay transitions to coupling neutron and proton orbitals with the same l quantum number, dramatically reducing the number of transitions that are favored. Nuclei with magic numbers of protons will need to promote the decaying neutron to a state above the proton shell gap, and the angular momentum numbers of that next proton orbital will dictate which valence neutron orbitals would be able to populate that proton state. These decays would incur a steep energy penalty corresponding to the size of the shell gap. Similarly, neutron transitions from mismatched orbitals are forbidden and suppressed by the angular momentum considerations mentioned previously. These twin effects lead to the observed stability against beta decay that characterizes magic nuclei.

Of particular interest in this model, then, are non-magic nuclei that are one proton below a magic number. In the ground state, these nuclei will have the same decay characteristics as the nearby magic nuclei, but with additional low-lying transitions that are possible on account of the hole in the proton shell. Transitions populating this hole will have similar angular momentum considerations to transitions populating states in the next proton shell but will not face the same

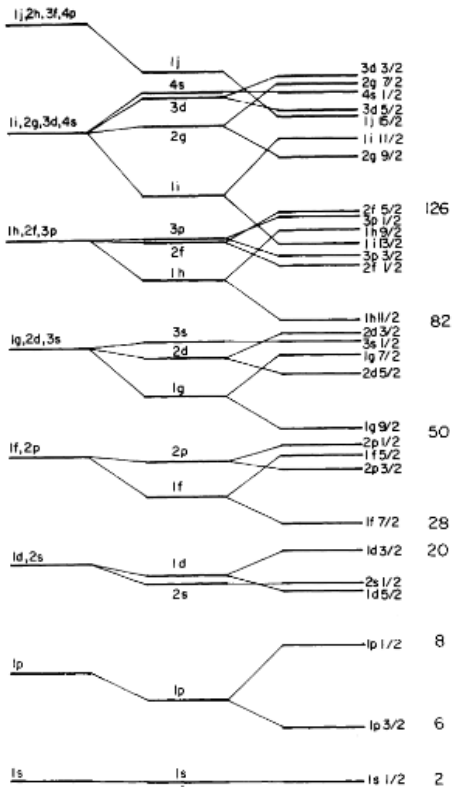

Figure 4: Nucleon orbitals according to the shell model. Splittings between these orbitals give rise to the familiar magic numbers at the right (Talmi, 1993).

energy penalty as those decays. Decay spectra from these nuclei are thus expected to show a distinct signature of a low-lying, high-intensity set of transitions to states below the proton shell gap, then a lower-intensity set of transitions to states above the proton shell gap with a notable energy gap between the two sets of transitions corresponding to the size of the shell gap.

Chapter 3: Experiment at NSCL

This experiment was carried out at the National Superconducting Cyclotron Laboratory (NSCL) on the Michigan State University campus. The NSCL is an accelerator facility that uses the fragmentation process to produce radioactive ion beams (RIBs). The resulting ion beams contain a cocktail of isotopes with similar masses and nuclear charges, which are implanted into a detector array and allowed to decay so that spectroscopy can be performed on the decay products.

3.1 Beam Production

Beam production at the NSCL uses the fragmentation process, in which a heavy, stable isotope is accelerated to form the primary ion beam. This primary beam is directed onto a light, dense, stationary target so that an abrasion reaction can occur, producing high-velocity fragments of the primary beam with diverse Z and N.

To select fragments by the desired values of Z and N, the reacted beam is transported into an electromagnetic separator. The Lorentz force law provides that a constant magnetic field B will direct a charged particle into a circular path with radius ρ given by $mv^2 = ZvB$, where m is the mass, Z is the charge, and v is the velocity of the charged particle. This can be rearranged to give $B\rho = mvZ$, with the quantity $B\rho$ being called the "magnetic rigidity" of the field. Fragments with higher momentum or with lower Z will thus have a larger radius of curvature for the resulting trajectory, allowing for the dispersion of fragments by momentum as they travel along the curved trajectory. The electromagnetic separator uses large dipole magnets to accomplish this separation (Figure 5).

Fragmentation reactions produce fragments that have kinetic energies roughly proportional to their mass, so their velocities are all approximately equal. Since the momentum of the fragments is thus proportional to their mass, the dipole magnets disperse the beam fragments by their mass-charge ratios m/Z on reaching the I2 position in the A1900 separator.

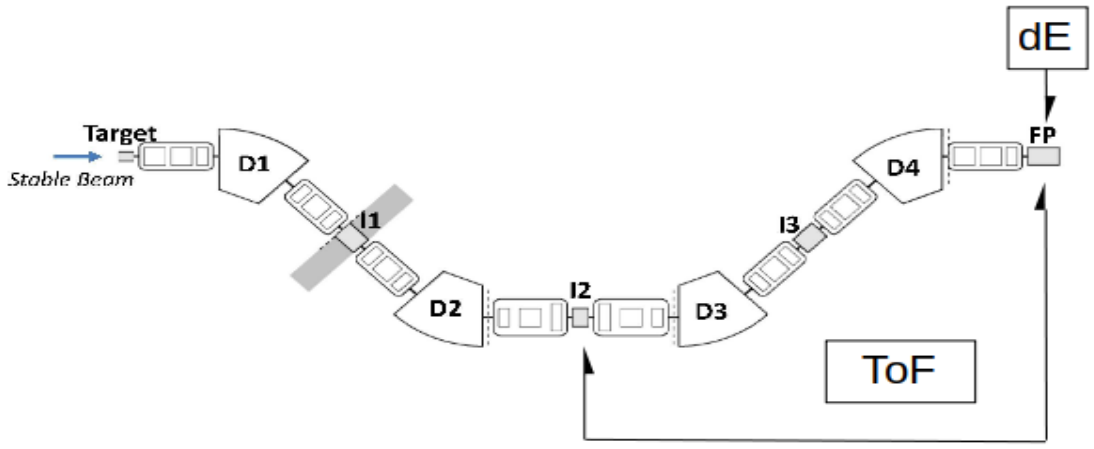

Figure 5: Schematic of A1900 fragment separator. D1-4 are the Dipole magnets. I2 is the dispersive plane of the separator, where the wedge degrader is placed. Marked are the measurements used for constructing the PID plot. Adapted from (Ginter et al., 2016)

Upon reaching the I2 position, the fragments are passed through a degrader to introduce an explicit Z dependence to the distribution of the fragments. Particles with energy *E* passing through matter with thickness *x* experience an energy loss given by $\frac{dE}{dx} \propto \frac{Z^2}{E}$. The resulting change in velocity of the fragments varies inversely with the initial velocity and directly with the thickness of the degrader, so a wedge-shaped degrader is chosen to introduce a mass-dependent, and therefore Z-dependent, variation in the velocity distribution of the fragments, as the initial velocities were all approximately equal. Downstream from the I2 position, the dipole magnets can then be tuned to a new $B\rho$ setting to selectively focus fragments with the desired Z and $\frac{m}{Z}$ to the focal plane of the separator, with other contaminant fragments now focused elsewhere and filtered out before reaching the experimental vault.

For this experiment, the primary beam consisted of ^{82}Se ions accelerated to 140 MeV/u and was fragmented on a target of ^{9}Be. The D1 and D2 magnets were set to a $B\rho$ setting of 4.25383 T·m, and the D3 and D4 magnets were set to a $B\rho$ of 4.19580 T·m. These settings were chosen to deliver isotopes with Z between 26 and 30 and $A/Z \cong 2.6$, primarily $^{70\text{-}72}$Co. Here $A = \frac{m}{m_u}$, where m_u is the nucleon mass.

3.1.1 Particle Identification

Beam production via the fragmentation method produces RIBs that are isotopically mixed. Accurately identifying the isotopes in the beam as they reach the experimental setup is essential for removing the effects of other isotopes from the measured decay spectrum. This is accomplished by a pair of measurements, one determining the $\frac{A}{Z}$ of the fragments, the other determining the Z of those fragments.

Measurements

Following the introduction of the velocity variation in the beam fragments at I2, the resulting velocities of the particles can be measured to determine their relative values of $\frac{A}{Z}$. This

is accomplished by measuring the Time of Flight (ToF) of the fragments between I2 and the experimental vault. The presence of the fragments at I2 is recorded using a signal from a small plastic scintillator, and the presence of the fragments at the experimental vault is measured with a silicon PIN just upstream of the experimental setup. A Time-Amplitude Converter (TAC) is used to measure and record the time difference between those two signals, from which the relative velocities of the fragments can be determined.

To determine the *Z* of the fragments, the Silicon PIN detector upstream of the experimental setup is used. Fragments passing through the PIN deposit energy according to the Bethe-Bloch formula as above. The PIN detector produces a signal that is proportional to this energy loss, which can be used to determine the *Z* of the fragments passing through it. Figure 5 shows the placement of the PID measurements.

I2 Position correction

Since the time measurement used to determine the velocity of the beam particles begins when the particles cross the dispersive plane of the A1900 separator, the distances covered by the various fragments are slightly different. Specifically, high-momentum fragments travel a slightly longer flight path, while low-momentum fragments travel a shorter distance, leading to a smearing in the PID plot. By detecting where in the I2 scintillator each fragment begins, a linear correction to the velocity measurement can be applied to correct for this smearing. In this experiment, two methods were attempted to apply this correction. The first attempted a direct measurement of the position of each fragment as it passed through the I2 scintillator can be computed by measuring when the scintillation light from the interaction reached opposite ends of the scintillator. The position of the interaction within I2 is then given by:

$$x_{I2} = c_{I2} * T_{diff}$$

Where c_{I2} is the speed of light within the I2 plastic and T_{diff} is the measured time difference between when the light reaches each end of I2. Since the variation in the position x_{I2} is small compared with the overall length of the flight path, a linear correction of the flight path by x_{I2} will be sufficient to correct the smearing and recover clear definition of the individual isotopes in the PID plot.

In this experiment, two methods were used to measure T_{diff}. The first used a TAC connected to each end of I2 to directly measure the time difference. The second used a pair of ToF measurements from I2 to the PIN detector in the focal plane, with one ToF measurement originating from each end of I2. The time difference between these two ToF measurements would correspond to the T_{diff}. While these two methods will generally give the same result, the beam rate passing through I2 resulted in a significant amount of deadtime for the TAC connecting the ends of I2, resulting in a significant loss of statistics after applying this linear correction via the first measurement. Since the second method only recorded ToFs for fragments that were delivered to the experimental setup, the rates on these TACs were much lower, so the second method suffered significantly less from deadtime issues and preserved much more of the PID dataset for use in subsequent analysis. The results of the correction procedure can be seen in Figure 6.

PID verification

^{78}Zn has an 8^+ isomer state (Daugas et al., 2000) with a half-life of 319 ns. Observation of the gamma rays from the de-excitation of this excited state allows for a verification of the PID isotope assignments (Figures 7 and 8).

3.2 Experimental Setup

The experimental setup consisted of a position-sensitive scintillating implant detector and downstream scintillator to use as a light ion veto within the beamline (see **Section 3.2.2**) (Figure 9). A pair of upstream Silicon PIN detectors and Time-Amplitude Converters (TACs) are used in Particle Identification (see **Section 3.1.1**). 42 medium VANDLE modules are placed in a cylindrical arrangement above the implant detector at a 1-meter flight path to provide neutron detection, and an array consisting of 1 high-purity Ge Clover, 12 HAGRiD ($LaBr_3$) detectors, and 8 NaI detectors are arranged below the beamline to provide gamma-ray detection.

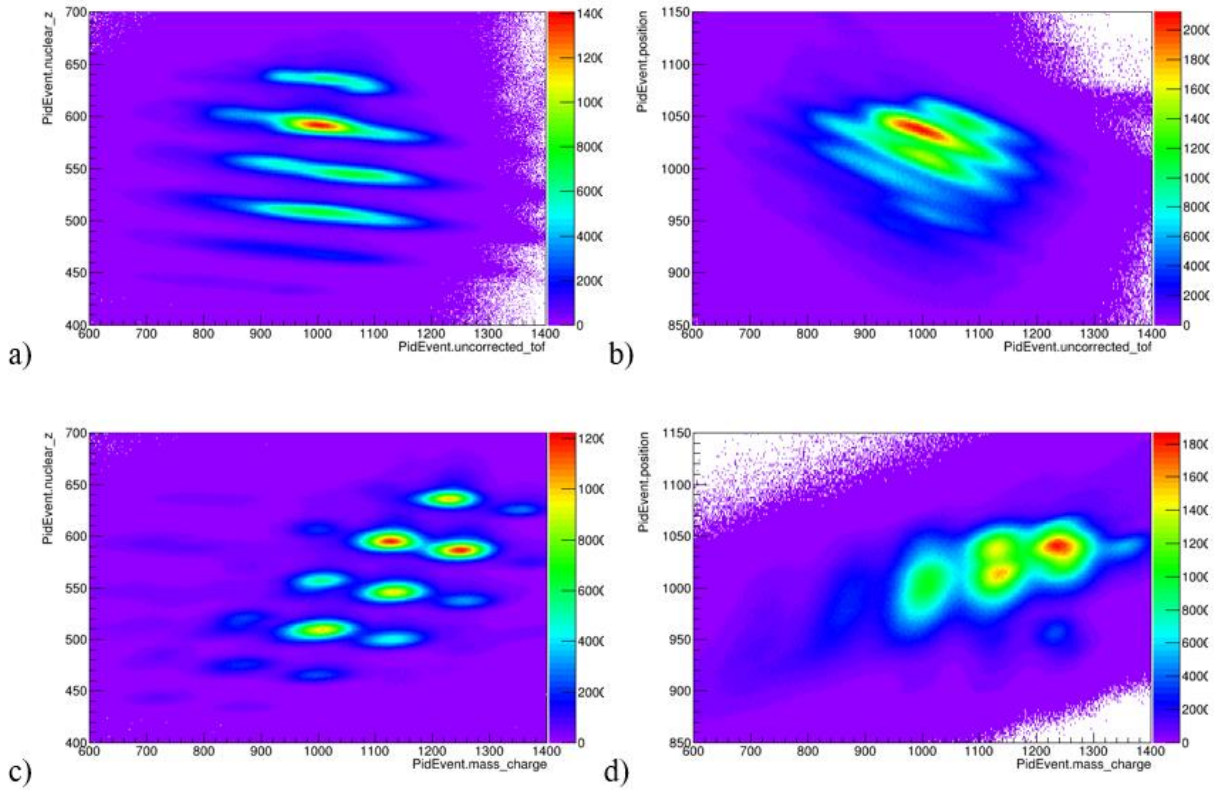

Figure 6: Particle Identification plot correction. Each axis displays arbitrary units. In (a), there is clear differentiation of isotopes by Z along the vertical axis, but the horizontal axis shows no definition of unique A/Q. The observed smearing is due to variation in the flight paths of the isotopes. (b) plots position in I2 on the vertical axis, illustrating the effects of this variation by position in the I2 scintillator on the ToF measurement, with the distinct bands of A/Q showing significant overlap in time of flight. Performing a linear correction to the ToF by the position detected in I2 scintillator gives definition to the PID plot (c), by realigning each A/Q band to a single ToF (d).

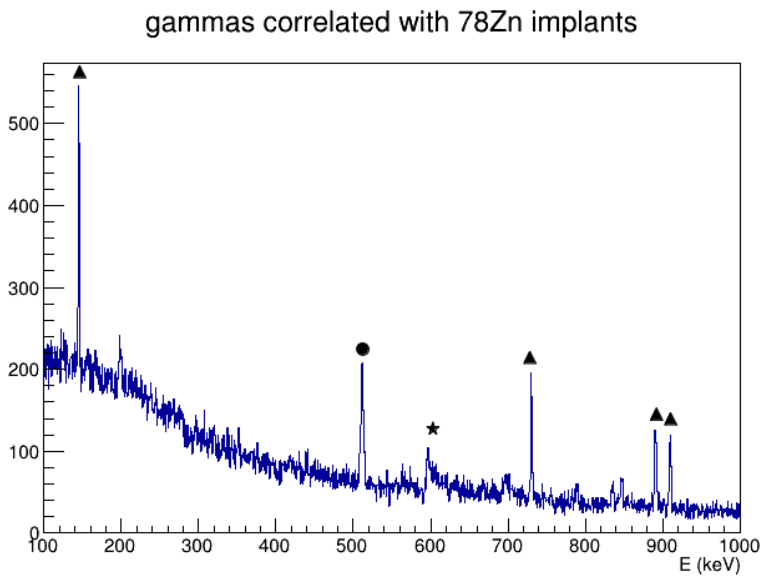

Figure 7: Gamma rays gated on implants of ^{78}Zn. ▲ indicates the gamma ray cascade from the 8+ isomer, with energies of 144 keV, 730 keV, 890 keV, and 908 keV. ● indicates pair production gamma rays (511 keV), while, ★ indicates a signature of (n,n') interactions in the Clover.

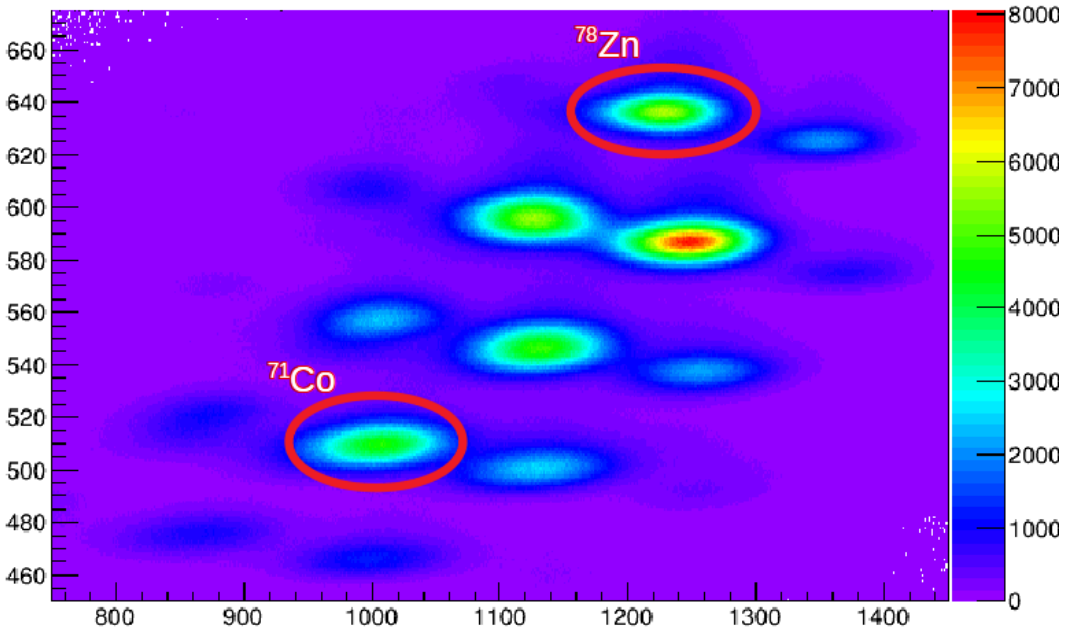

*Figure 8: PID plot with isotopes of interest marked. ^{78}Zn is used to verify the PID assignments and for characterizing the background decay rate (see **section 4.3**)*

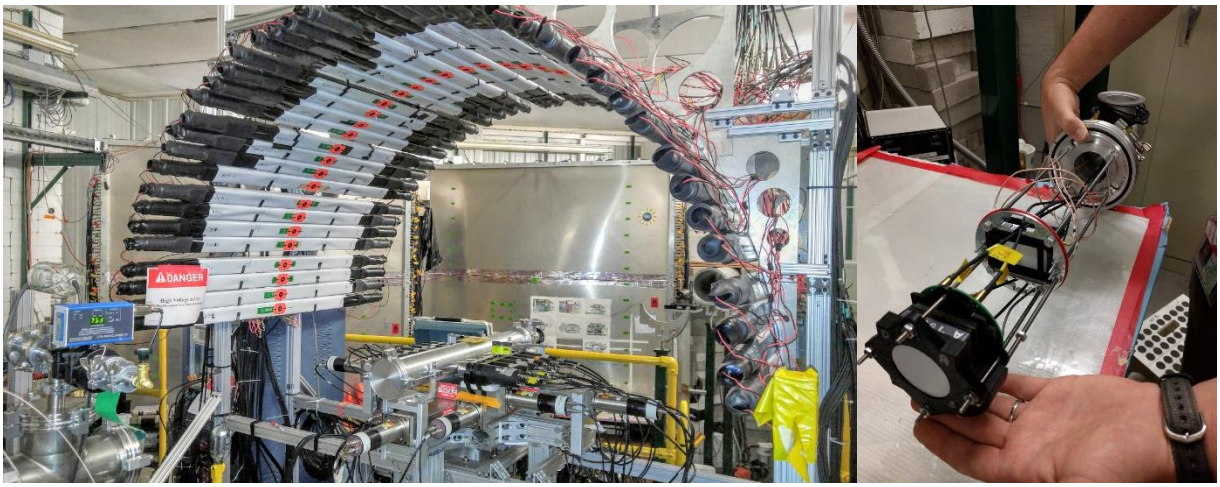

*Figure 9: Experimental setup at the NSCL. (***Left***) Above the beamline, 42 VANDLE modules are arranged in a cylindrical arc. An array of close-packed gamma ray detectors are placed below the beamline. (***Right***) Within the beamline is the position-sensitive implant detector and scintillator that serves as a light ion veto.*

3.2.1 VANDLE

The Versatile Array of Neutron Detectors at Low Energy (VANDLE) (Matei et al., 2009; Paulauskas et al., 2014; Peters et al., 2016) is a modular array of neutron detectors that uses the Time of Flight (ToF) technique to perform neutron spectroscopy. It is most often used in measurements of beta-delayed neutron emitters (Paulauskas, 2013; Taylor, 2018), but has also been deployed in (d,n) reaction measurements (Thornsberry, 2018).

Principles

The Time of Flight technique is used to provide high-resolution energy measurements of particles by measuring the time it takes for the particles to traverse a known distance (Figure 10). For VANDLE, the ToF measurement is the time difference between a beta decay in the implant detector and a subsequent neutron event in one of the VANDLE bars. By detecting the position of the neutron impact with the VANDLE bar as well as flight time of the neutron following the beta decay event, the energy of the neutron can be computed.

$$E = \frac{1}{2}mv^2 = \frac{1}{2}\left(939.57\frac{MeV}{c^2}\right) * \left(\frac{r}{ToF}\right)^2$$

When a neutron scatters in a VANDLE bar, scintillation light is produced that propagates the length of the bar and is detected at the bar ends by a pair of photomultiplier tubes. Since the light propagates along the length of the bar at a consistent speed, the position *x* of the neutron interaction along the length of the bar can be computed from the time difference (T_{diff}) between the light signals from the photomultiplier tubes:

$$x = c_{bar} * T_{diff}$$

where c_{bar} is the speed of light in the VANDLE plastic. T_{diff} is defined by convention as the left side of each bar minus the corresponding right side, such that a negative T_{diff} corresponds to an interaction upstream of the implant point, while a positive T_{diff} corresponds to a downstream

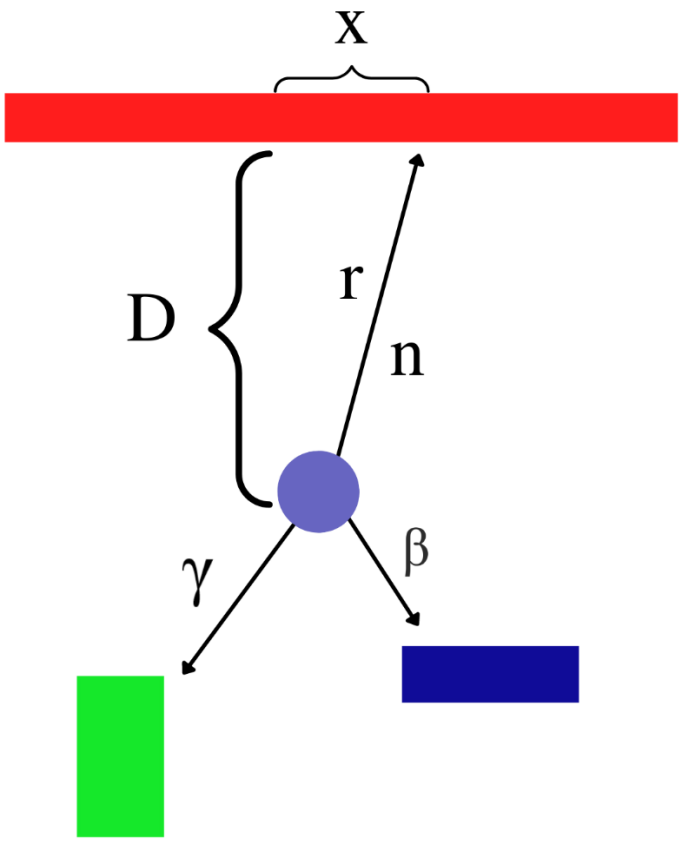

Figure 10: Schematic of the VANDLE ToF technique. The ToF measurement begins with a beta decay which is detected by the beta-detection system (blue), and then ends with a coincident neutron event in the VANDLE plastic (orange), set a distance D *away from the beta detector. The position of the neutron within the VANDLE plastic (*x*) allows for the proper construction of the full flight path (*r*). Any gamma rays that are coincident with the beta decay and neutron must also be detected (green) to accurately reconstruct the excitation energy of the emitter nucleus.*

interaction. Since the VANDLE modules form a cylindrical geometry around the implant detector, the flight path of the neutron from the implant detector to the point of detection within the VANDLE bar is given by the Pythagorean Theorem:

$$r^2 = x^2 + D^2$$

D is the distance from the implant detector to the center of the VANDLE bar.

The uncertainty in the energy measurement is given by:

$$\frac{\delta E}{E} = \left(\left(2\frac{\delta r}{r} \right)^2 + \left(2\frac{\delta ToF}{ToF} \right)^2 \right)^{\frac{1}{2}}$$

Here δToF is the timing resolution of the ToF system, including both the intrinsic VANDLE timing resolution and the time resolution of the implant detector. The uncertainty δr is primarily determined by the width of a VANDLE bar.

Construction of VANDLE detectors

Each VANDLE module consists of a bar of Eljen EJ-200 plastic scintillator optically coupled at each end to a Hammamatsu model R7724 photomultiplier tube (PMT). VANDLE modules come in several sizes (small, medium, large). This experiment made use of 42 of the medium VANDLE modules, which measure 120 cm in length, 6 cm in width, and 3 cm in thickness. These VANDLE modules were arranged in a cylindrical arc above the implantation point for the RIB at a distance of 1 m.

Each VANDLE bar is wrapped in two layers of aluminized mylar. The inner layer of mylar is double-sided, while the outer layer is single-sided. These two layers serve to optically isolate the plastic from the environment, both preventing scintillation light from escaping the plastic without being seen by the PMTs and keeping external light from the experimental environment from leaking into the plastic and drowning the scintillation light (Figure 11).

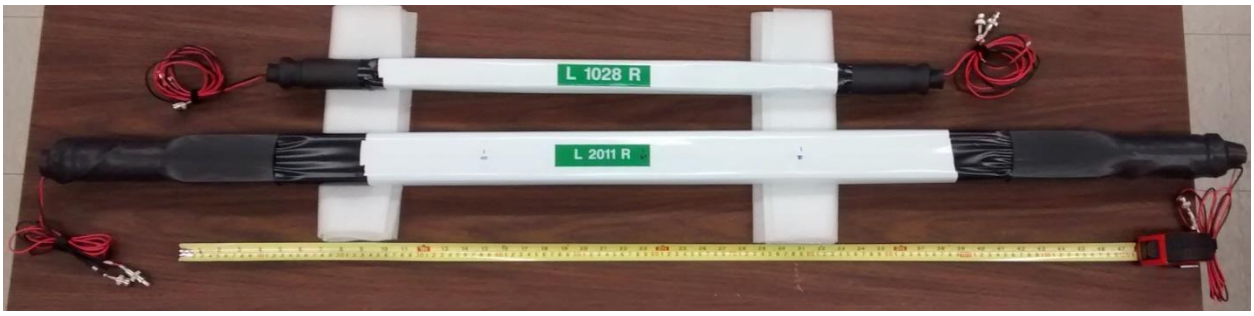

Figure 11: Assembled small and medium VANDLE modules.

Digital Data Acquisition

VANDLE makes use of a digital Data Acquisition system (DAQ) to record signals from the experiment for offline analysis (Paulauskas et al., 2014). Photomultiplier signals are digitized and recorded using a set of 12-bit Pixie16 digitizer modules sampling at 250 MHz. Digitizing signals from the detectors allows for signals to be revisited in offline analysis and the performance of sophisticated post-processing. Particularly in this experiment where time resolution is an important limit on the overall energy resolution, digitization of the signals from the VANDLE and implant photomultipliers also allows for significant improvements over the nominal 4 ns timing resolution that the digitizer clock frequency would give. This is accomplished by fitting the signal traces with a custom function and then interpolating the precise time that the signal crosses the triggering threshold. In this experiment, this interpolation procedure improves the timing resolution to 1.8 ns overall. (Paulauskas et al., 2014)

Neutron detection efficiency

VANDLE's plastic scintillator has a linear relation between the energy deposited in the plastic by a neutron and the amount of scintillation light that is produced. For neutrons that deposit energy below a certain threshold, insufficient light will be produced to create a valid VANDLE trigger. Even above this detection threshold, a neutron may fail to sufficiently interact with the VANDLE plastic as it passes through the bar, leading to a failed detection event. For this reason, accurately characterizing VANDLE's detection efficiency over a range of energies is an essential step in identifying and accounting for these failed detection events.

To provide an intrinsic measure of VANDLE's detection efficiency, a medium VANDLE bar was tested at the Edwards Accelerator Laboratory at Ohio University (Peters et al., 2016). A well-characterized ^{27}Al(d,n) reaction was used to produce neutrons with a known energy distribution, which were then detected by the VANDLE bar 11 m from the reaction point. Comparing the detected neutron distribution with the neutron distribution produced by the reaction, and normalizing based on solid angle coverage of the bar, gives an intrinsic efficiency curve for a single VANDLE bar.

In this experiment, VANDLE covered a total of 19% of 4π in solid angle. However, the overall efficiency is also affected by the gain settings of the VANDLE photomultipliers. To account for different gain settings used in different experiments, and differing detection thresholds, GEANT4 simulations can be used to model VANDLE's efficiency curve for other gain settings. It is observed that these simulations systematically over-predict the neutron efficiency by about 17% compared to the measured efficiency curve. While the cause of this discrepancy is presently not well understood, it is easily accounted for by scaling down the simulated efficiency curves by 85%. With these corrections, the full experimental setup can be simulated to produce the overall VANDLE efficiency curve.

To produce the neutron efficiency curve, the full experimental setup is constructed in GEANT4. An isotropic, monoenergetic neutron source is placed in the center of the setup to simulate the production of delayed neutrons, and the number of neutrons detected by the system is recorded and compared to the total number of neutrons produced by the source. Neutrons with a variety of energies between 200 keV and 5 MeV were produced and recorded. The resulting distribution was fit with a 4th degree polynomial and scaled by the aforementioned 85% to produce the overall neutron efficiency curve for the experiment (Figure 12).

Neutron response function

Due to the ways neutrons interact with material in the experimental hall, monoenergetic neutrons will show a characteristic distribution of Times of Flight in VANDLE instead of a single, sharp ToF peak. This distribution can be described by a response function of the detector to neutrons of a specific energy, which must be tuned to properly reproduce the neutrons from the long-ToF tail of the distribution. The full experimental setup is modeled in GEANT4 and monoenergetic neutrons are produced at the implantation point to simulate the neutron ToF distributions. In this case, distributions of neutrons with energies of 500, 1000, 2000, 3000, 4000, and 5000 keV were generated. For each of these monoenergetic distributions, a piecewise function consisting of an asymmetric Lorentzian peak and three exponential tails is fit to the distribution.

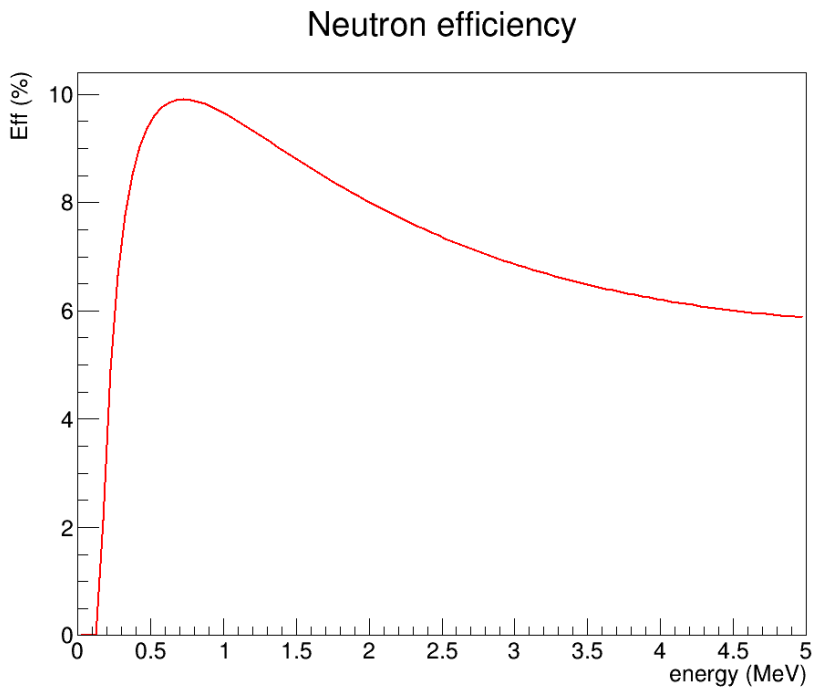

Figure 12: Simulated neutron efficiency curve for the experimental setup.

The fitting parameters are then extracted from each monoenergetic fit and a polynomial is fitted to each parameter to describe the relationship between the ToF centroid of the distribution and the various parameters of the response function. These polynomials allow for the construction of a neutron response function for any neutron energy in VANDLE that can be used to decompose the continuum neutron distribution into distinct energy states.

3.2.2 Position-sensitive beta detection

Historically, VANDLE has been employed in decay experiments performed at facilities that use the Isotope Separation On-Line (ISOL) beam purification technique. ISOL uses a light primary beam incident on a heavy target to induce fission in the target. The fission fragments are then re-accelerated for delivery to the experimental setup, which gives ISOL facilities the ability to produce isotopically pure beams, since the momentum of the resulting fragments is a function of their charge, not their mass. This means that the beta-detection system VANDLE uses to produce the start signal for the neutron ToF measurement at an ISOL facility can be relatively simple. The beams produced in the fragmentation reactions at the NSCL, however, are isotopically mixed, so the beta-detection system needs to be able to discriminate between implants of several different isotopes to avoid cross-contamination of results. Further, since the resulting beta decay activity will be a mix of all of the previously implanted isotopes, the beta detection system will need to be designed to enable correlating a beta decay event with a preceding implant event on a case-by-case basis

Detector Design

Position-sensitive Silicon Strip Detectors (SSDs) are typically used as beta detectors in decay experiments at fragmentation facilities, but silicon-based detectors do not have the requisite timing resolution to give a good VANDLE start signal (M. Alshudifat et al., 2015). For this reason, a scintillator-based detector was developed (Figure 13). It consists of a solid, Cerium-doped Yittrium Aluminum Perovskite (YAP:Ce) crystal, coupled to a quartz light guide

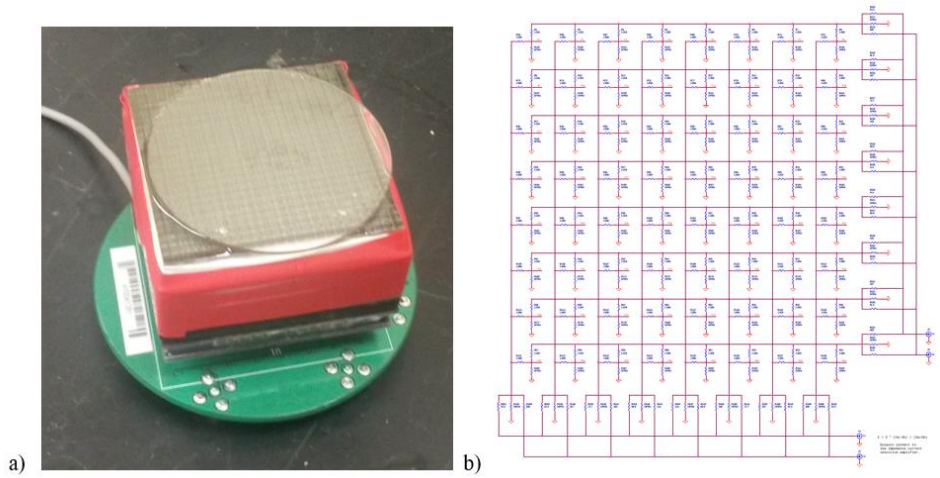

Figure 13: Design of the implant detector. (a) The assembled detector. (b) Schematic showing the resistive readout for the PSPMT. Each anode signal is divided into x and y positions. These positions are then read out through a pair of resistors, with the relative impedances dictated by the position of the photomultiplier segment along the relevant axis.

consisting of a 24 x 24 grid of 2 x 2 mm^2 segments. The light guide is further coupled to a Hamamatsu H12700A-03 array, consisting of 64 square photomultiplier segments. The electrical signals from the array are read out through an Anger logic resistor network, reducing the outputs to 4 anode signals containing the position information and a common dynode signal for timing. A similar design had been used in an experiment at Tokai (Xiao et al., 2019).

Ion-beta tagging and triggering scheme

The beta-detection system needs to be able to discriminate between three different kinds of events in order to be effective. Isotopes from the beam implanting into the detector and subsequent decays of those isotopes need to be identified and correlated to produce a proper decay spectrum for the isotopes of interest. These two kinds of events can be differentiated by the presence or absence of a coincident signal from the PIN detector used to create the PID plot. The position-sensitive nature of the detector allows for correlations to be made between these two kinds of events, so valid implant and decay events will require signals from all 4 position anodes and the common dynode. Implant events will also require the presence of a signal from the upstream PIN detector indicating the presence of the implanting isotope in the PID plot, while decay events will necessarily lack this coincident signal.

The fragmentation process also produces a large quantity of high-energy light ions that may reach the implant detector. These implants of light ions may not produce a signal in the PIN detector, thereby mimicking decay signals as they punch through the implant detector. An additional scintillator is included in the beamline of the experimental setup downstream from the implant detector to detect and properly identify events attributable to these light ions and so veto them from the analysis. Some light ions may nevertheless fail to be properly vetoed, perhaps due to scattering and thereby missing the veto detector. The effects of these ions can be clearly seen in the decay-gated dynode signal of the implant detector (Figure 14).

Removing the effects of these remaining light ions while leaving the underlying distribution of beta particles intact is potentially non-trivial and has the potential to impact the overall beta-detection efficiency of the implant detector (see **section 3.3.5**)

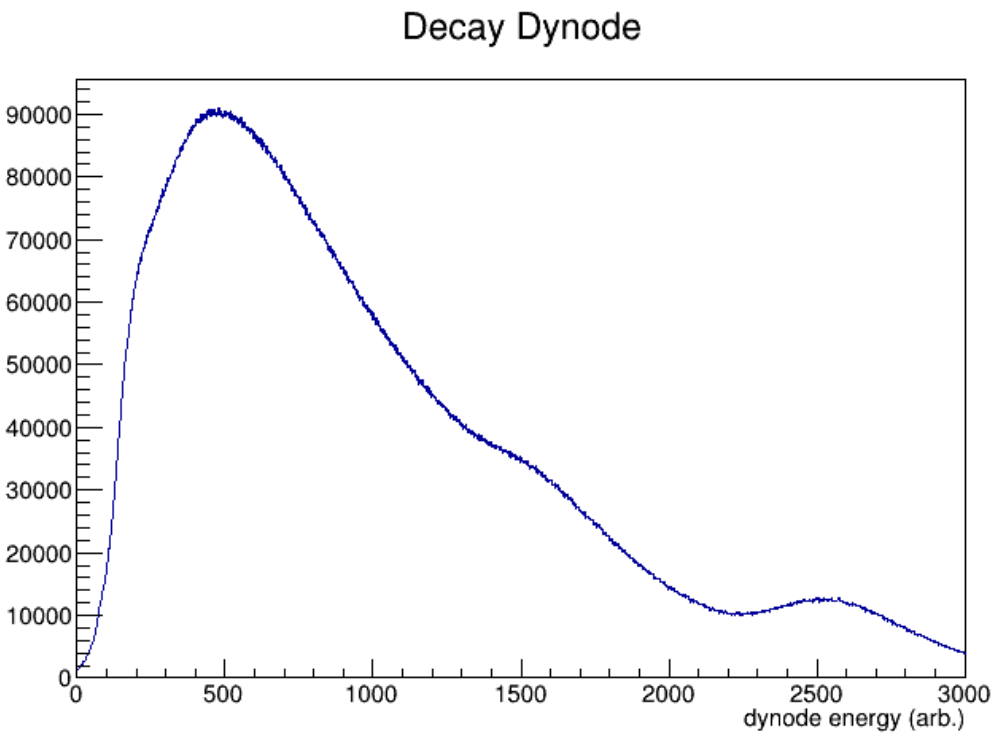

Figure 14: Distribution of decay-gated dynode energies. Though light ions from the fragmentation process are vetoed out, the remnants of peaks around 1500 and 2500 ADC units are still present, corresponding to impacts of protons and deuterons, respectively, with the face of the detector.

For the VANDLE measurement, the beta-decay trigger provides one part of the coincidence trigger for the delayed neutron measurement from VANDLE. The VANDLE trigger that serves as the other portion of the measurement consists of a logical OR of pairwise ANDs of the VANDLE PMTs corresponding to each VANDLE bar. This overall coincidence requirement enables the use of a low threshold on the VANDLE PMTs, since room background that would otherwise appear in VANDLE will be sharply reduced by the coincidence requirement.

Position correction

The implant detector uses an Anger logic algorithm to reconstruct the positions of events in the detector. Signals for the x- and y- positions are split and then attenuated proportionately to the position of the event along the axis in question. The x- and y- coordinates of the event positions can then be recovered via the following first-order formulae

$$x = \frac{x_a - x_b}{x_a + x_b}$$

$$y = \frac{y_a - y_b}{y_a + y_b}$$

where the subscripts *a* and *b* represent the first and second signals from each axis, respectively (see Figure 13b).

This algorithm gives an accurate relative reconstruction of event positions in the implant detector, but correlations between high-energy implant events and lower-energy beta-decay events are hampered by several effects. The first is that the implant detector exhibits a non-linear response to the scintillation light, causing a shrinkage of the reconstructed detector face for the higher-energy implant events compared with the lower-energy decay events. Second, the implant detector shows significant edge effects, causing further crowding and distortion of the pixel positions near the edges of the detector face (Figure 15). For this reason, modifications to the position formulae need to be applied in order to be able to more consistently correlate pixels between implant and decay events.

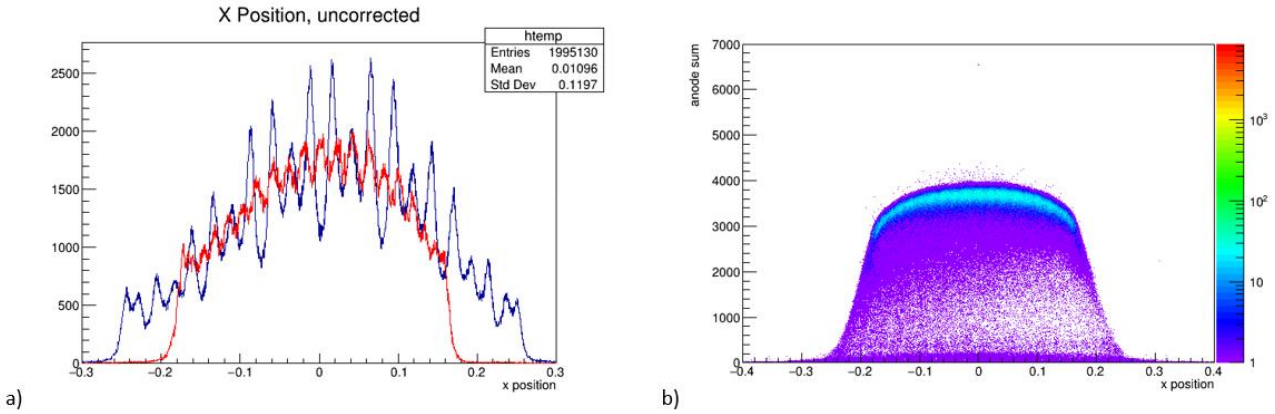

Figure 15: Plots showing the non-linear distortion of x positions in the Implant detector. a) shows a comparison between implant events (red) and decay events (blue). Implant counts are scaled by a factor of 3 relative to decays for ease of comparison. Even though clear evidence of pixelation exists in both position distributions, corresponding pixels are not aligned properly. b) shows the energy dependence of the effect for implant events, with higher-energy events along the vertical axis displaying a noticeably smaller detector footprint than lower-energy events.

The first modification is applied to the high-energy implants to re-scale and re-align the implant pixels to the decay pixels. This is accomplished by adding small next-leading-order correction terms to the Anger logic position formulae for the implant gate, yielding

$$x_{implant} = \frac{x_a - x_b + c(x_a^2 - x_b^2)}{x_a + x_b + c(x_a^2 + x_b^2)}$$

$$y_{implant} = \frac{y_a - y_b + c(y_a^2 - y_b^2)}{y_a + y_b + c(y_a^2 + y_b^2)}$$

Here ***c*** is a free parameter that controls how much the higher-energy positions are scaled relative to the lower-energy ones and can be tuned to provide good alignment between the observed pixels (Figure 16). This correction produces good position agreement for the central pixels of the detector but is insufficient to correct the pillowing effects near the edges.

Correcting the edge effects requires applying a further transformation to the positions, of the form $x' \rightarrow b * \tan\left(\frac{x}{a}\right)$ where *(x,y) = (0,0)* is the center of the detector. ***a*** and ***b*** can be tuned to control the magnitude of the re-spacing applied to the edge pixels relative to the effect on the center pixels. Applying this correction widens the correlatable face of the detector significantly, leaving only the very edge-most pixels as unresolvable (Figure 17).

Position correlation

Due to the isotopically impure nature of the fragmentation process, multiple different isotopes will be implanted into the detector setup. Each of these isotopes will produce decays that will contribute to a high background decay rate. To reduce this background as much as possible, decays are correlated with preceding implants only if they occur within the same or a neighboring pixel as the implant in question, and only then if the decay also occurs within 260 ms of the implant. The time window of 260 ms is chosen to allow for approximately 3.5 half-lives of ^{71}Co (~80 ms) to elapse, so the majority of the relevant implants will have the opportunity to decay within that timeframe (Rajabali et al., 2012; Sawicka et al., 2004).

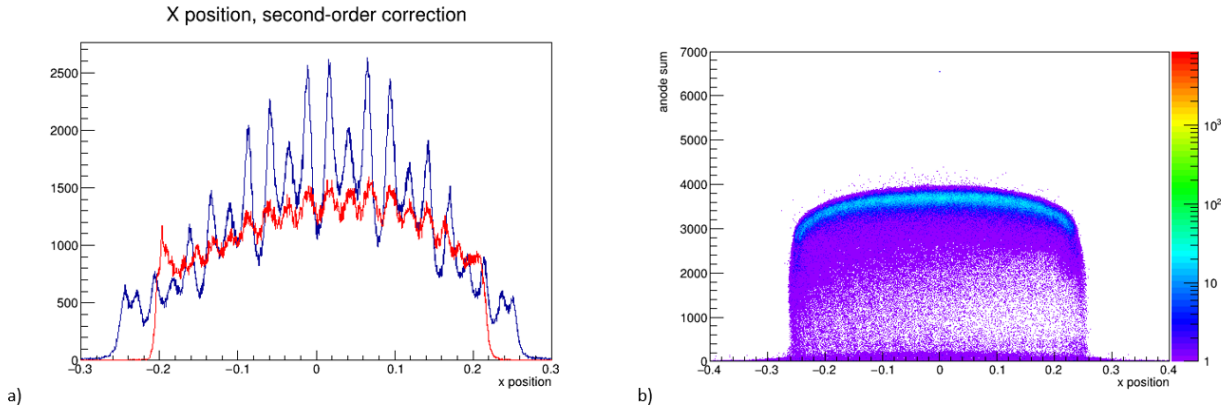

Figure 16: Event positions in the implant detector after applying the second-order correction to the position formula. As in Figure 15, a) shows a comparison between the x positions of the decays (blue) and the implants (red), with the implants scaled by a factor of 3. b) shows the effect of the correction as a function of energy, with a much-reduced energy dependence. This correction shows good agreement between the implant and decay pixels out to about 6 pixels from the center.

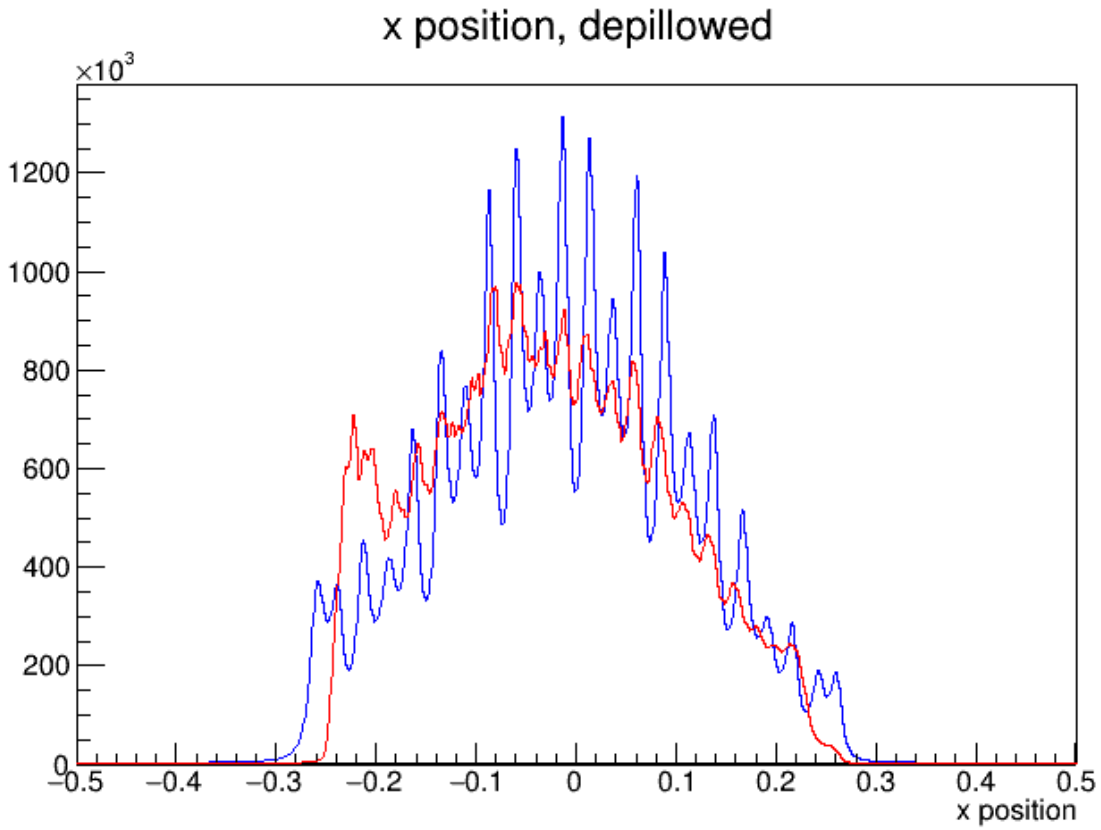

Figure 17: X positions in the implant detector following the depillowing process. The depillowing process reclaims about 3 pixels on each side of the distribution relative to applying just the 2nd-order correction to the positions. Implants (red) are scaled by a factor of 3 relative to decays (blue) for ease of comparison.

Candidate decay events are identified by looking back through past implant events to see if an eligible implant event occurred within that timeframe (see **section 4.1**). Plotting these candidate decay events by the time elapsed between them and their corresponding implant allows for the construction of a decay curve for the nucleus in question (Figure 18). Due to the high implant rate on the order of 1000 particles per second, the background decay rate in the implant detector, which is comprised of half-lives on the order of 100s of ms, equilibrates with the implant rate in a matter of seconds, and so can be considered to be constant over the course of the experimental runtime, simplifying the fitting procedure considerably.

Beta efficiency

The beta-detection efficiency of the implant detector can be measured by integrating the decay curve for a given nucleus and comparing the number of correlated decays to the corresponding number of implants in the active face of the detector. This beta detection efficiency represents the proportion of beta-decay events that interact within the YAP which could provide a valid start signal for the neutron ToF measurement.

However, the remaining presence of light ions in the beta decay gate will introduce distortions to further analysis by slightly increasing the nominal beta decay count but greatly increasing the number of neutron-like events in the VANDLE ToF spectrum (Figure 19). Placing a gate on the dynode to remove the effects of these light ions will also remove some of the high-energy beta signals, reducing the overall beta efficiency, and potentially affecting the detected neutron events by removing some otherwise valid decays from consideration.

To characterize the effects of the light ion removal, several cuts were made on the decay dynode (see Figures 15 and 19). The cuts were spaced every 100 ADC units beginning at 400 and ending at 2000. 400 ADC units is below the peak in the beta spectrum so the first few points would show the effects of severe beta removal. It was also expected that the effects of proton-induced particle events would appear in the ToF spectrum beginning around 1300 ADC units, so the last several points would be expected to show the effects of allowing the light ions to remain in the analysis.

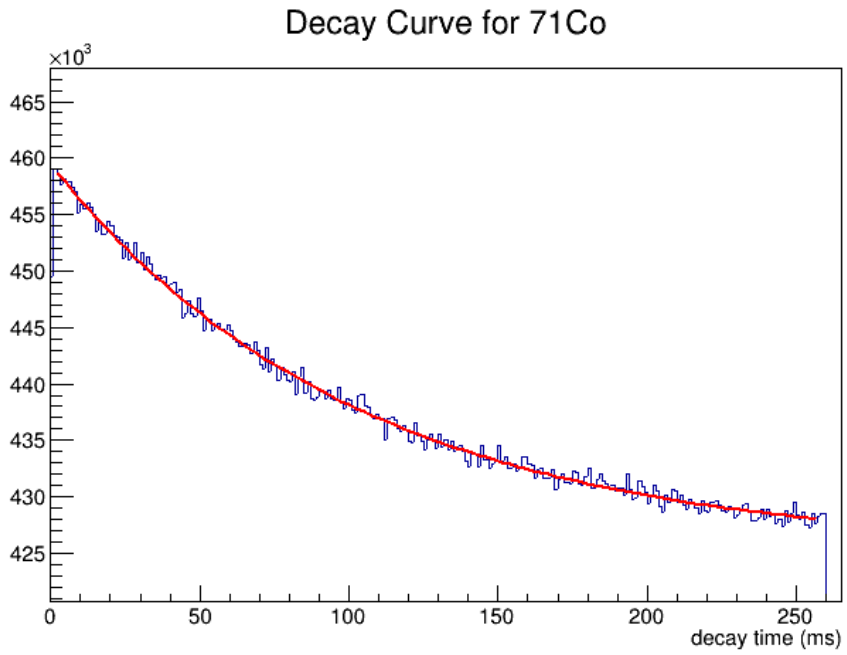

Figure 18: Decay curve for ^{71}Co decays. The background decay rate is reduced by applying a correlation radius of neighboring pixels between implants and corresponding decays but remains high due to the large number of other decaying isotopes in the detector. The decay curve here shows a half-life of 74.7±1.7 ms, which is faster than but still consistent with the values observed by (Sawicka et al., 2004) *and* (Rajabali et al., 2012).

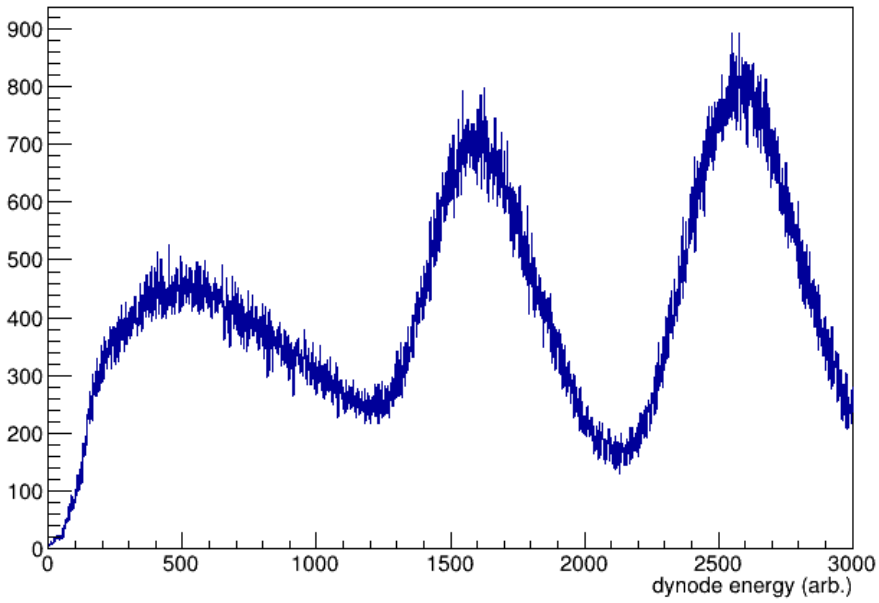

Figure 19: Neutron-gated dynode. Gating on the particles detected in VANDLE cuts out the large number of beta events that are correlated with gamma rays seen in VANDLE. it does not, however, significantly remove VANDLE events caused by light ions that aren't successfully vetoed. Since these light-ion-induced particles will mimic neutrons in VANDLE, cuts on the dynode are needed to remove the effects of these particles.

For each of these dynode cuts, the analysis procedure detailed in **Chapters 4 and 5** was carried out to determine the nominal P_n value the cut would give. Figure 20 shows the plot of the measured P_n value against the placement of the dynode cut. For cuts below the proton peak, the P_n value is relatively insensitive to the cut placement. This behavior suggests that these cuts are not producing major distortions in the neutron spectrum, as the number of neutrons in the ToF spectrum is scaling linearly with the increased beta efficiency. Once cuts begin to include portions of the proton peak, the nominal P_n increases greatly relative to the beta efficiency. This increase is due to the large number of proton-induced particles that are detected by VANDLE, so failing to remove even a small amount of them has a significant effect on the resulting neutron spectrum. As expected, this increase begins to manifest with the cut at 1300 ADC units, while the cut at 1200 ADC units shows no effects of light ion presence. This indicates that a cut on the dynode at 1200 ADC units will completely remove the remaining light ions without negatively distorting the eventual ToF spectrum. This dynode cut results in a beta efficiency of 39%.

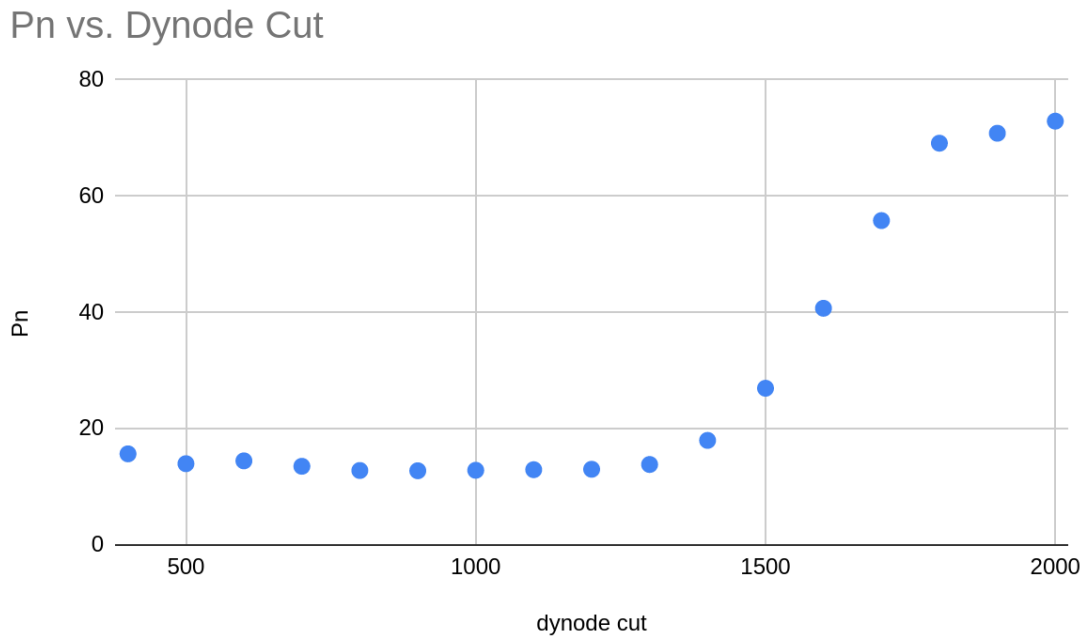

Figure 20: Nominal P_n vs. decay dynode upper limit. Dynode cuts that exclude the proton peak show a linear scaling between the beta efficiency and the number of neutrons detected in VANDLE, which results in P_n being insensitive to the placement of the cut. Beginning at 1300 adc units, the intrusion of proton-induced effects in VANDLE results in a sharp increase in the nominal P_n value, indicating the outsize influence that these protons have on the resulting VANDLE spectrum.

Chapter 4: Analysis

4.1 Event Building and corrections

The first step of the analysis process is reading and packaging the detector signals for further analysis. For this purpose, an in-house analysis suite called the Pixie Acquisition and Analysis Software Suite (PAASS) is used. PAASS is a C++ based, modular software suite that analyzes and packages the various detector signals together into 5 μs events. PAASS scans the raw signal data and opens an event when it encounters the first signal. Once the event is open, all signals with timestamps within the following 5 μs window are collected together into the same event. After 5 μs, the event is closed and the next signal marks the opening of the next event.

PAASS has modules that perform specific analysis on signals from specific detectors. These include processes such as energy calibrations for the gamma ray detectors, the computation of event positions within the implant detector (**Section 3.2.2**), and the construction of the PID plot.

VANDLE events undergo several specific analysis steps here. The position of each event within the bar is computed, and the ToF is determined by the difference between the high-resolution time of the decay event recorded by the implant detector and the high-resolution time of the VANDLE event itself. The ToF is then normalized to a 1 m flight path, which corrects for several effects. First, the axial geometry of the VANDLE bars introduces up to a 16 cm variation in the flight path of the neutrons that will result in smearing of the eventual ToF distribution. Second, while each bar is set at a nominal distance of 1 m from the implant detector, small variations in the construction of the detector frame introduce a variation of a few cm of jitter to the flight distance to each bar. Correcting each ToF to the same nominal length means that each ToF bin will correspond to a single, well-defined energy instead of varying by the flight path of the neutrons, alleviating both of these potential problems. Third, it is observed that the propagation speed of light within the VANDLE plastic shows an energy dependence. This results in the geometrical correction, which assumes a constant speed of light in the VANDLE bar, will insufficiently correct the ToFs of higher-energy particles. Adding an energy

dependence to the propagation speed allows for the correction of this problem (Figures 21 and 22).

Once this pre-processing using PAASS is done, a second stage of analysis is performed. The list of events is parsed into implant, decay, and veto categories, as described in the triggering logic section of **section 3.2.2**. Then, for each valid decay event, a vector of implants within a one-pixel radius of the decay over the preceding 260 ms is constructed. 260 ms corresponds to about 3.5 half-lives of ^{71}Co, so in this timeframe approximately 91% of the implanted ^{71}Co ions are expected to decay. Each implant event contains the relevant PID information of that isotope as well as the position and timing information from the implant detector, so that correlations involving isotopes of interest can be selected. Each decay event will likewise contain the position and timing information from the implant detector and will also include any coincident Clover and VANDLE events.

Specific implant-decay correlations are made on a decay-by-decay basis by looking back through the vector of correlated implants for a specific implant of interest within the correlation radius and decay window. Correlating in this manner raises the number of background decays that are included in the correlation gate but avoids the risk of double-counting neutrons for which there are multiple valid implants due to each decay event only being considered once. Two different gates are used to make correlations, one based on implants of ^{71}Co, the other based on implants of ^{78}Zn to be used as a background spectrum (see **section 4.3**). Once the list of properly correlated decay events is compiled, the VANDLE events coincident with those correlated decays can be analyzed.

4.2 VANDLE spectra

Figure 23 shows the VANDLE spectrum for this correlation procedure. The low-QDC band of events are random, uncorrelated, low-energy background events that clear the VANDLE threshold. The banana-shaped structure that rises out of these background events between about 35 and 200 ns on the horizontal axis are the decay-delayed neutrons and light-ion-induced

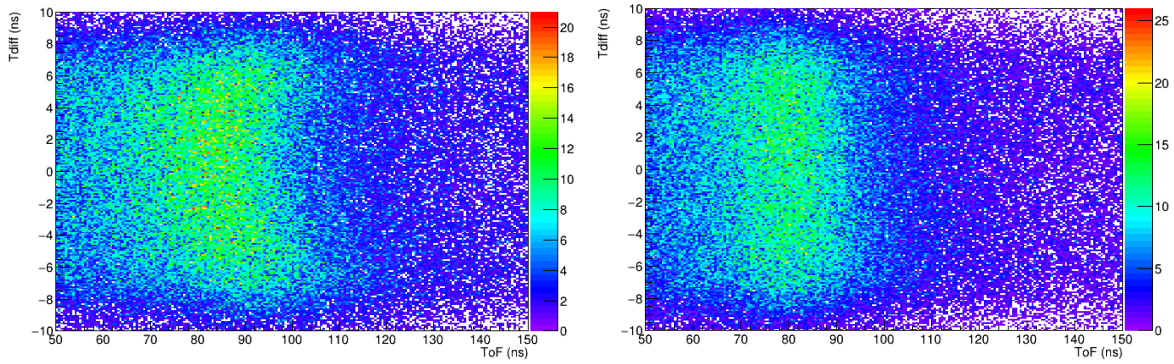

Figure 21: Plot of VANDLE axial position vs. ToF. (left) plots the bar Tdiff against the uncorrected ToF, showing that the bar edges have a bias towards longer ToFs, due to the longer flight path from implant detector. (right) Normalizing the ToF to a consistent 100 cm flight path removes this bias.

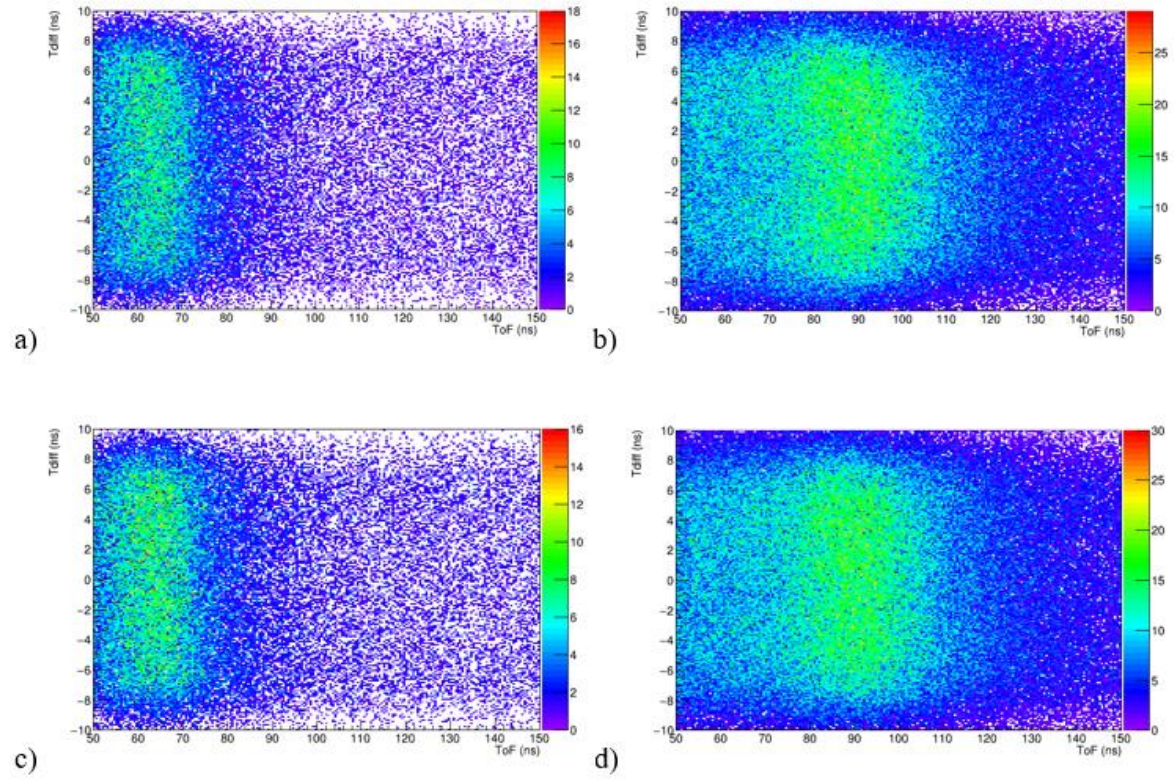

Figure 22: QDC-dependent ToF Correction. A purely geometrical correction to the VANDLE ToF (see figure 21) is sufficient for aligning the ToFs of high-energy neutrons (a), but over-corrects the ToF for low-energy neutrons (b), biasing the bar edges towards shorter ToFs. Applying an energy-dependent correction to the propagation speed of light within the VANDLE bar allows for consistent alignment regardless of energy (c-d).

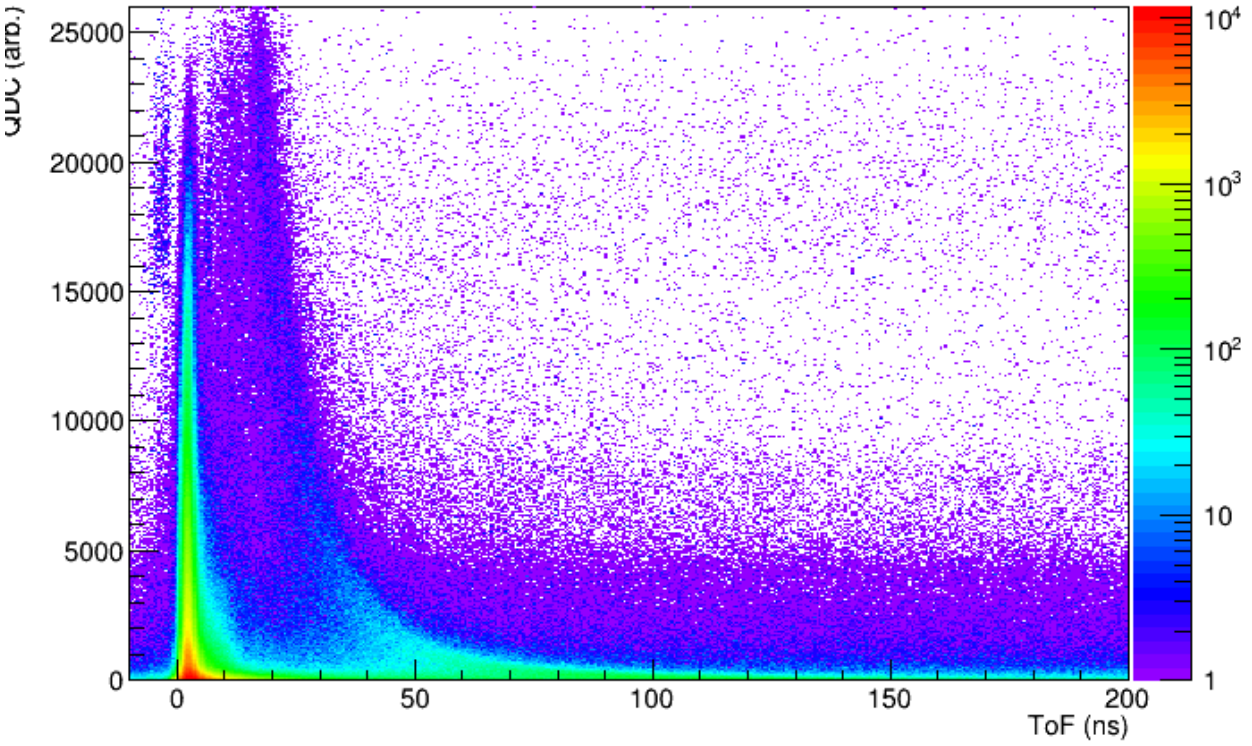

Figure 23: QDC vs ToF VANDLE spectrum. The fast vertical structure is the prompt gamma flash, and the banana-shaped structure is neutrons. Evidence of additional partial flashes and particle structures can be seen smearing to the left of the main structures. These are attributable to light-ion interactions with the upstream degrader, resulting in faster-than-expected ToFs.

reaction products. Particles with shorter ToF are higher-energy, and so have more energy to deposit in the VANDLE plastic, raising the structure of the neutron distribution above the band of low-energy background events. The prompt peak is the flash of gamma rays from decays that are detected by the VANDLE plastic.

The analysis in the beta efficiency portion of **section 3.2.2** indicates that the majority of the particles observed in the VANDLE spectrum are attributable to light ion effects, which can be removed with a cut on the dynode signal. Placing this cut sharply reduces the number of errant high-energy particles in the banana structure and removes the hallmarks of the ion-induced reactions in the upstream degrader, such as the doubling of the high-energy gamma flash at a small negative ToF and the smearing of the particle banana toward shorter ToFs (Figure 24).

Since the prompt gamma rays all travel at a speed of *c* regardless of energy, the width of this peak can give an accurate measure of the overall time resolution of the experimental apparatus. Projecting the high-QDC portion of the gamma flash and fitting the resulting ToF spectrum with a Gaussian distribution gives a Full-Width at Half Max (FWHM) of 1.8 ns, which corresponds to the overall timing resolution of the VANDLE ToF measurement (Figure 25).

4.3 Background Characterization

Random correlations resulting from decays of other isotopes from the ion beam will quickly equilibrate with the implant rate and result in a flat background for the decay curve. However, several of these isotopes are also delayed-neutron emitters, and so neutrons from these decays will appear in the neutron ToF spectrum alongside neutrons from the isotope of interest, washing out the neutron spectrum due to the high rate of background decays relative to the decays of interest.

To properly characterize this background decay rate, a decay spectrum gated on ^{78}Zn is also prepared (Figure 26). ^{78}Zn is produced relatively abundantly in the ion beam, has a long half-life of 1.47 s, and has a virtually nonexistent neutron emission window of 400 keV (Sonzogni, 2007). This means that neutrons detected in coincidence with a decay of ^{78}Zn can be attributed to random background counts. The number of counts in the ^{78}Zn background spectrum

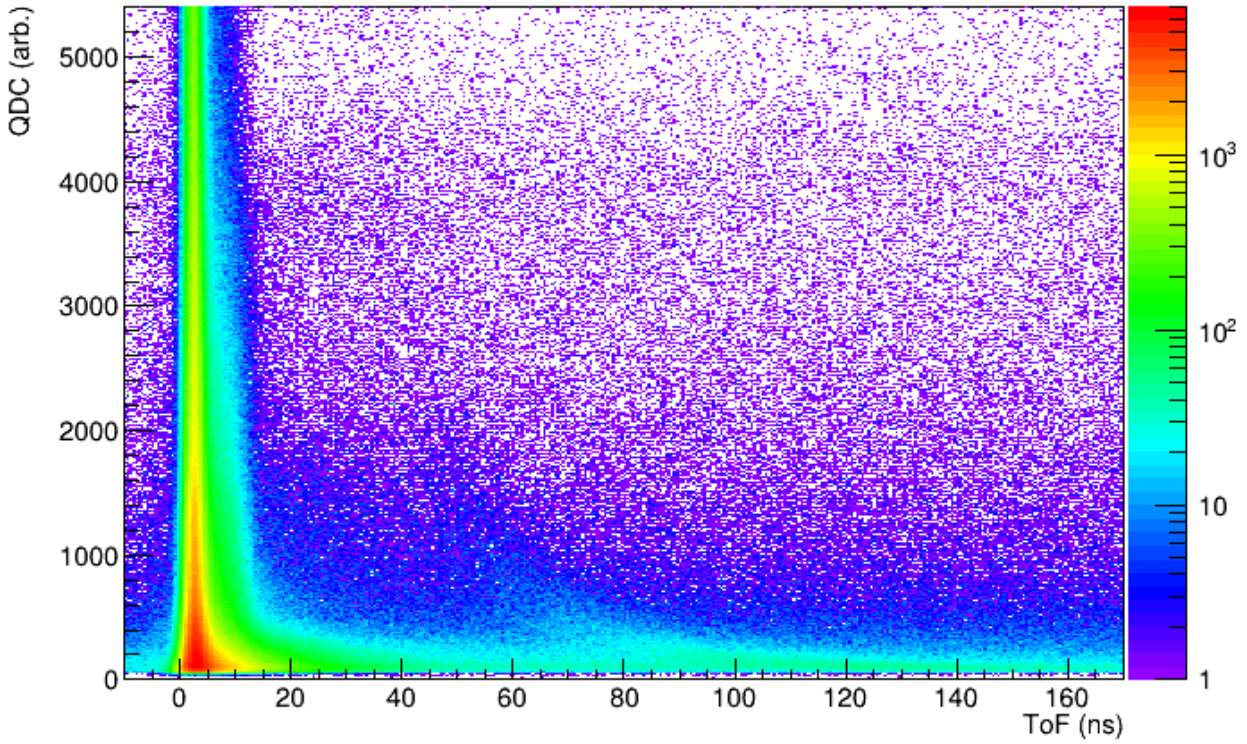

Figure 24: QDC vs ToF VANDLE spectrum after removal of light ion effects. The very-high-energy portion of the spectrum has been removed, as it was populated with light ion reaction products.

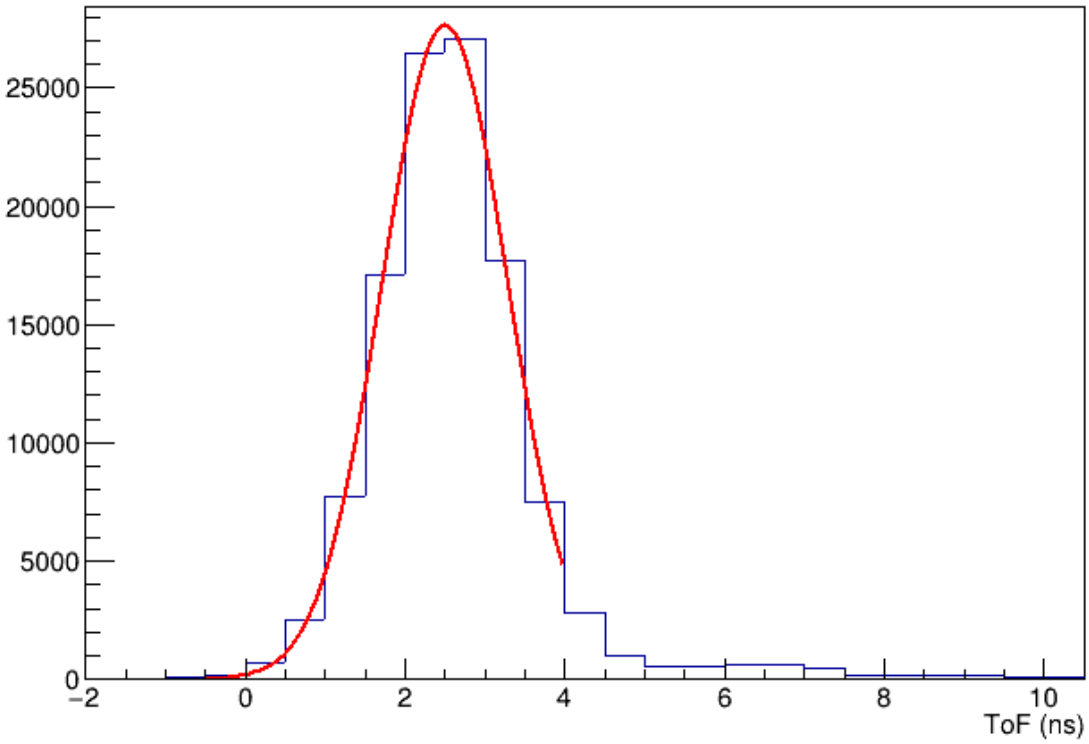

Figure 25: Gaussian fit of the gamma flash. The asymmetrical low-energy portion is removed by cutting below 10,000 QDC. This fit has a FWHM of 1.8 ns, defining the overall time resolution of the VANDLE measurement.

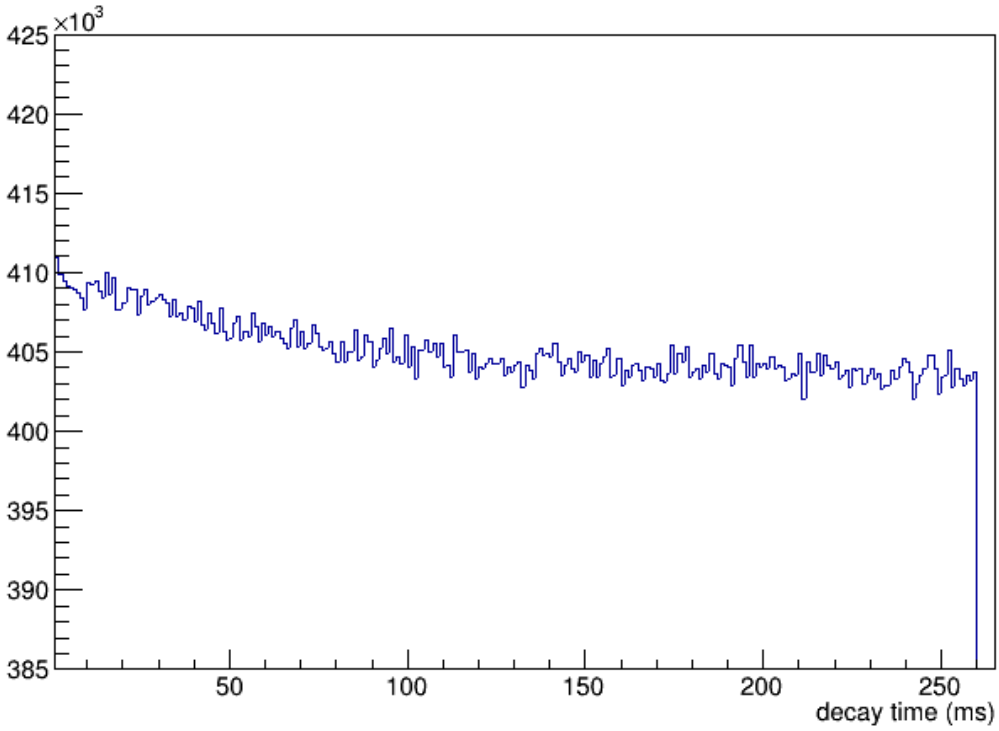

Figure 26: Decay curve gated on decays of ^{78}Zn. Due to the long half-life of ^{78}Zn relative to the decay window and the small neutron emission window, ^{78}Zn makes an ideal isotope to use in the construction of a background decay spectrum. The VANDLE events from this spectrum can be subtracted from the ToF spectrum from Figure 24 to produce the result seen in Figure 27.

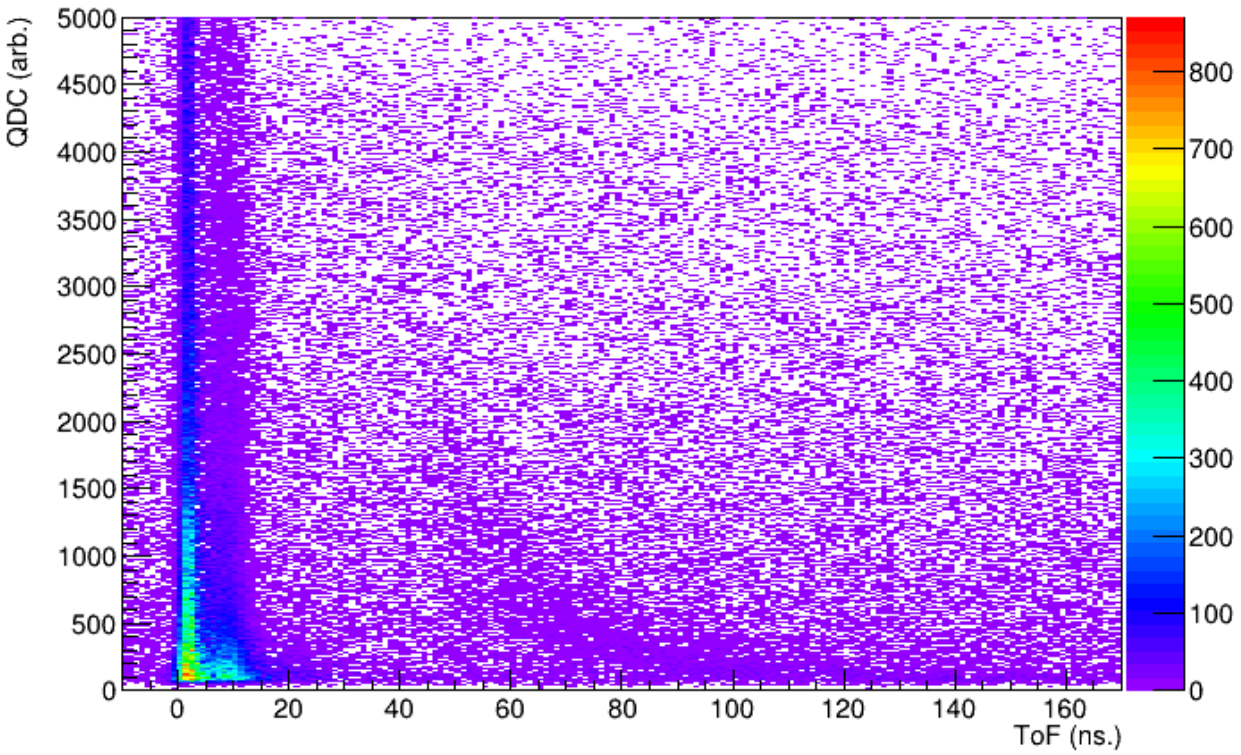

Figure 27: Background-subtracted ToF spectrum. The background subtraction significantly reduces the low-energy baseline and suppresses the intrusion of other β-n emitters into the spectrum. The doubled shape of the gamma flash peak is an artifact of the background subtraction. The lower-QDC structure around 10 ns has a different shape for different isotopes so the background subtraction procedure does not completely remove it. While the cause of the structure is not clear, it can be treated as part of the gamma flash for the purposes of the neutron fitting procedure, so it can be safely ignored.

is normalized to the flat background rate in the fit decay curve, and this normalization factor is used in subtracting the background neutron spectrum from the decay-gated neutron spectrum to create a background-subtracted neutron spectrum (Figure 27). Some kinds of background will nevertheless persist, such as the low-energy band of random correlations, but this subtraction has the effect of "cleaning" the implants by removing the effects of other neutron-emitting isotopes randomly correlating with the implants of interest.

Chapter 5: Results

5.1 Preliminary neutron deconvolution

To deconvolve the neutron spectrum for ^{71}Co, a high-QDC cut is made on the ToF spectrum, into which high-energy neutron peaks are placed to fit the selected portion of the ToF spectrum. Successively lower QDC cuts are then made, and the peaks are allowed to grow in intensity as the number of counts in the spectrum increases. As the QDC cut is lowered, lower-energy neutrons appear in the ToF distribution, for which additional, lower-energy neutron peaks are added to the spectrum. The resulting spectrum will illustrate the extreme case of all observed neutron emissions feeding the ground state of the granddaughter nucleus and will serve as a foundation upon which the final spectrum will be built. The results of this preliminary deconvolution can be seen in Figures 28 and 29.

5.2 P_n measurement

Once a deconvolution of the neutron spectrum is produced, the fit peaks can be integrated and corrected for VANDLE's experimental efficiency to give a total count of neutron emissions. This number is compared to the integrated decay curve, which indicates the total number of valid beta decay events, to provide a direct measurement of the neutron branching ratio P_n for ^{71}Co. Even though a final deconvolution will involve feedings to excited states in ^{70}Ni, this adjustment will not affect the observed distribution of neutrons within VANDLE, so it should not have a significant impact on the measured P_n value, though it can be refined by the final deconvolution. This preliminary fit gives a P_n value of 13.8%. The following section will refine this value to 14.0 ± 1.7%, consistent with the expectations here.

Previous attempts to constrain the P_n of ^{71}Co produced inconsistent results, with some (Rajabali et al., 2012) claiming to establish a 2.7% upper bound while others (Mazzocchi et al., n.d.) claiming to establish a 3% lower bound. These past studies sought to constrain the value of P_n using gamma-ray measurements, and so were necessarily insensitive to neutron branches populating the ground state. Since these past results observed an approximate 3% branch of

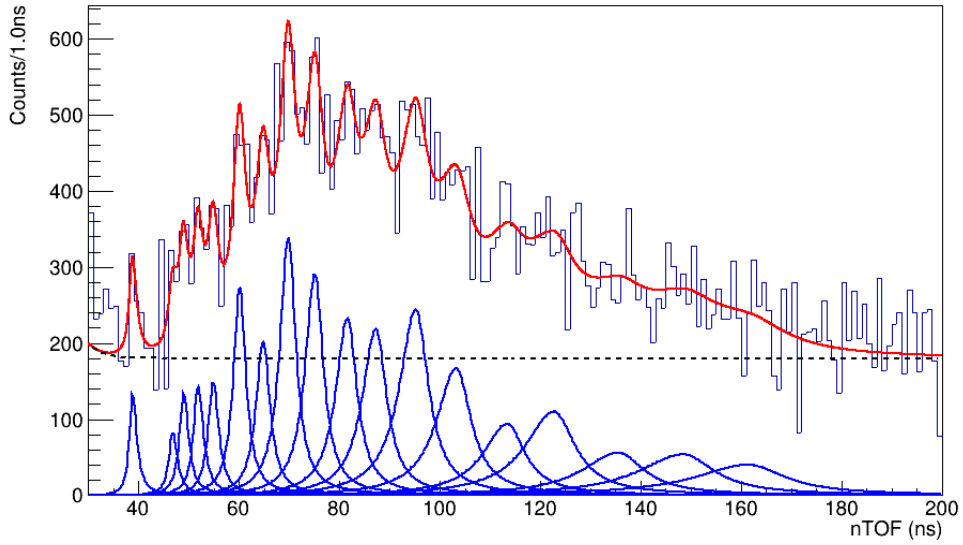

Figure 28: Deconvolution of the ^{71}Co neutron spectrum assuming only population of the ground state in ^{70}Ni. The active range for fitting is considered to be between 35 ns where the tail if the gamma flash disappears, and 185 ns where the VANDLE efficiency drops to zero.

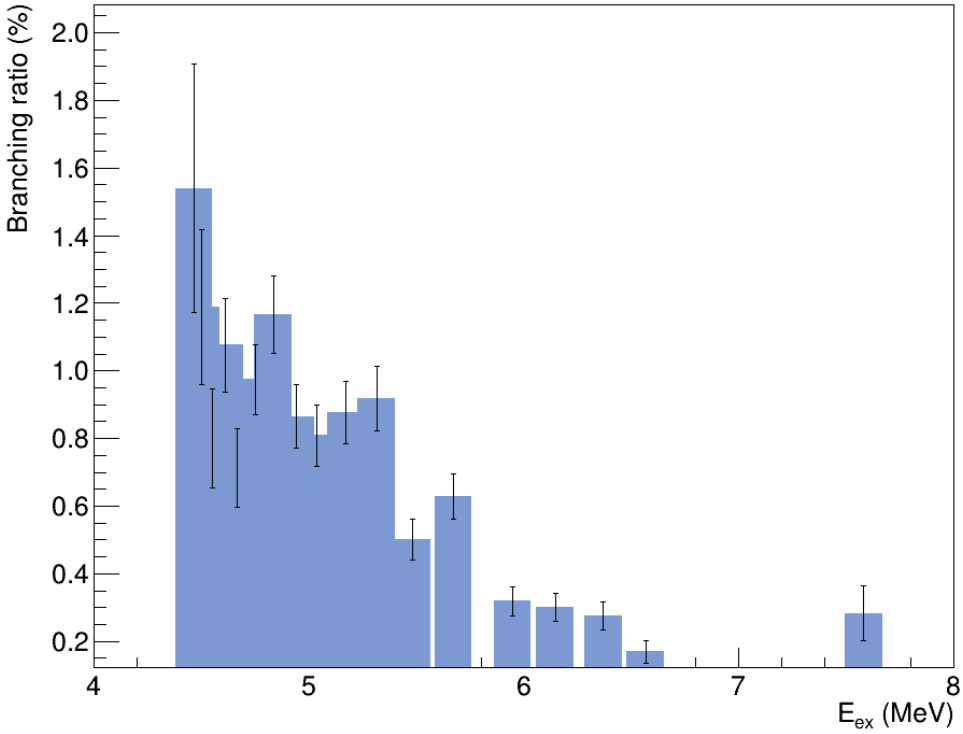

Figure 29: Plot of branching ratio for the neutron deconvolution assuming all transitions are feeding the ground state in ^{70}Ni.

decays coincident with a 1260 keV gamma ray, it is expected that a similar branch should be observed in this work. More recently, (Benzoni, 2016) presented a decay scheme for ^{71}Co that predicted a 16% P_n value, as well as feedings to several excited states in ^{70}Ni up to 3.5 MeV in excitation energy (Figure 30). Though this result has not yet been published and can only be treated as preliminary, it shows good agreement with the direct P_n measurement here and serves as a significant guide for the prediction of gamma ray coincidences below.

An additional consideration here is the prospect of neutron-gamma competition above S_n, of the kind observed by (Spyrou et al., 2016) for the case of ^{70}Co beta decay. Given the high measured P_n in this work, compared with the small gamma feeding above S_n observed by (Lyons et al., 2019) (see **section 5.4**), neutron-gamma competition seems to play a negligible role in the de-excitation of highly-excited daughter states in the decays of ^{71}Co.

5.3 Neutron-gamma coincidences

To account for neutrons feeding excited states in ^{70}Ni, a gamma ray spectrum gated on VANDLE events is created (Figures 31 and 32). Gamma rays from the ^{70}Ni daughter can then be identified and used as gates to produce neutron ToF spectra feeding through the corresponding excited state. Fits of neutron peaks to these spectra will serve to promote some number of neutrons from the prior ground state feeding to an excited state feeding.

As a guide for which excited states may be populated following neutron emission, a Hauser-Feshbach statistical model simulation is used to predict the relative populations of the excited states in ^{70}Ni (Figure 33). This calculation models neutron emission from states in ^{71}Ni with an excitation energy of 7,582 keV, and models feeding to states up to 3.2 MeV in ^{70}Ni. The three predominant states that are expected to be populated are the pair of 2+ states with energies 1260 keV and 1867 keV and the 4+ state with energy 2229 keV. The 0+ state at 1567 keV, the 6+ state at 2677 keV, and the pair of 5- states at 2912 keV and 3209 keV are populated much less strongly and are less likely to be seen with any sort of clarity in the data due to the significant amount of background in the gamma spectrum.

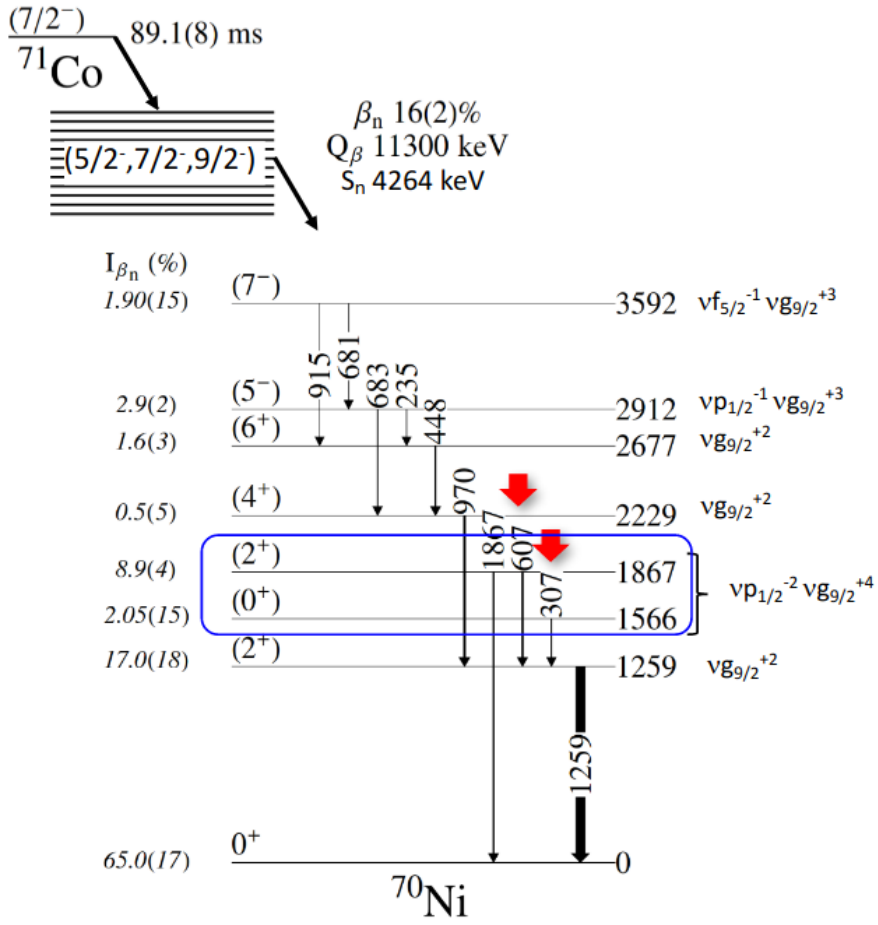

Figure 30: Predicted beta-delayed neutron feedings to excited states in ^{70}Ni. Due to limited statistics, not all of these transitions are expected to be observed in this work. Figure from (Benzoni, 2016).

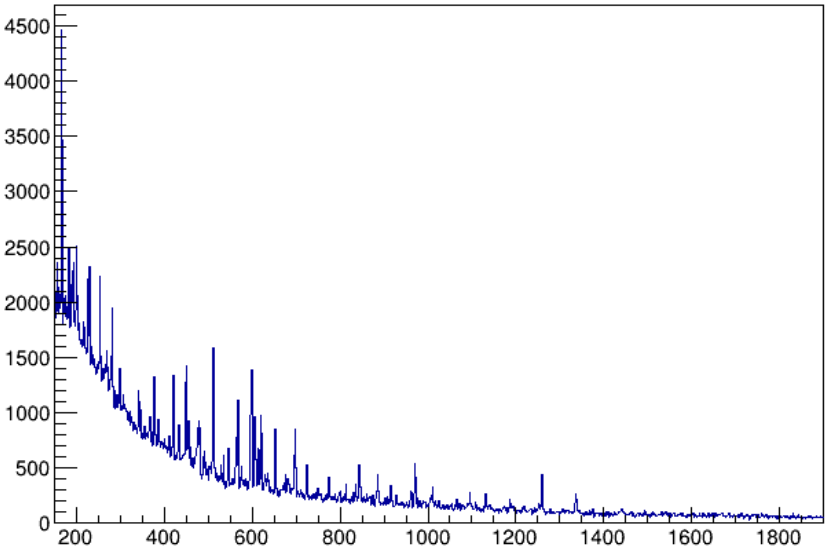

Figure 31: Gamma ray spectrum gated on ^{71}Co VANDLE events. This spectrum is not corrected for background, so the majority of the gamma rays observed here are from decays of other nuclei and appear due to a coincident gamma ray being detected by VANDLE.

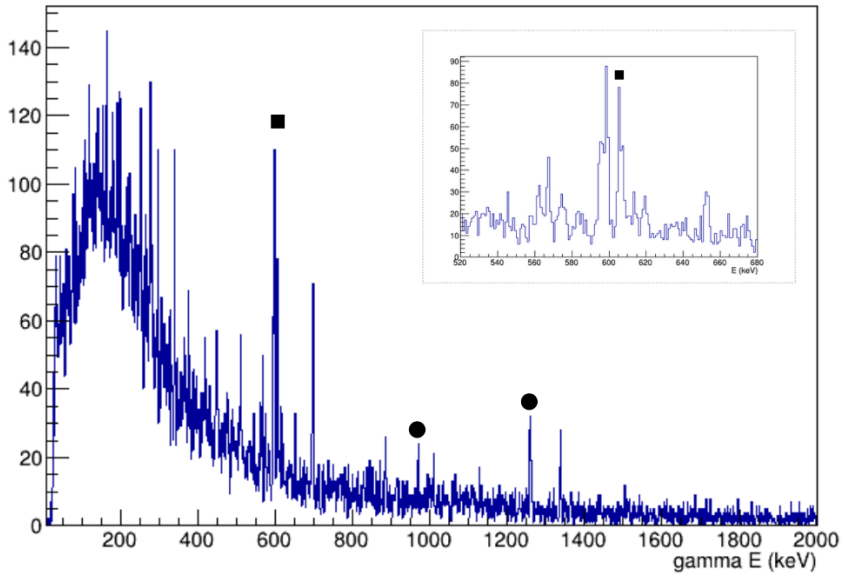

Figure 32: Gamma ray spectrum gated on ^{71}Co neutron events. This spectrum is a more restrictive gate than Figure 31, requiring the VANDLE event to have a ToF of between 35 and 200 ns. This gate removes all the random coincidences with the gamma flash, lowering the background peaks significantly. ● shows clear gamma rays from beta-delayed neutron emission of ^{71}Co (969 keV and 1260 keV). ■ indicates another likely gamma ray from beta-delayed neutron emission (607 keV), but this gamma ray shows evidence of contamination due to (n,n') effects on the Clover, and so cannot be reasonably fit. The inset shows a close-up of the (n,n') signature.

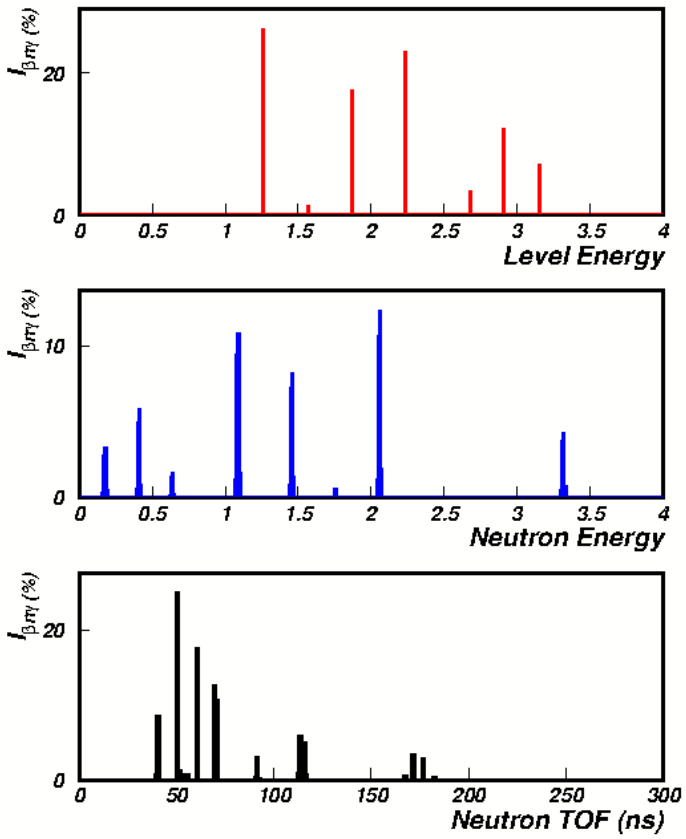

Figure 33: Hauser-Feshbach model (Okumura et al., 2018) *predicting neutron-gamma feedings in ^{70}Ni. The upper image shows the relative feedings to each excited state in ^{70}Ni following neutron emission from a 7582 keV excited state in ^{71}Ni. The lower plots show neutron energies and ToFs, respectively, for the neutrons emitted from such a state.*

Producing a gamma-gate deconvolution thus begins with the 2+ state (Ex 1260 keV) that was previously observed in (Mazzocchi et al., 2005; Rajabali et al., 2012). This state should have a significant direct neutron feeding according to the statistical model calculations and will also be indirectly fed by the states above it, so most branches to excited states in ^{70}Ni will eventually pass through this state. This spectrum is produced by taking a gate with an 8 keV width centered around 1260 keV, then subtracting a similar 8 keV-wide gate centered around 1232 keV, where the gamma detection efficiency is similar but no specific gamma rays are observed, to normalize the relatively large amount of background.

To fit the resulting spectrum, a two-part analysis is employed. First, candidate peaks are fit to the gamma-gate ToF spectrum. Second, these candidate peaks are scaled by the gamma detection efficiency and included in a fit of the full neutron spectrum to evaluate the agreement with the overall neutron deconvolution. The intensities of the gamma-gated peaks are allowed to vary to find the best fit agreement in the full neutron spectrum, but their relative intensities are kept fixed to maintain agreement with the gamma-gated spectrum. The resulting intensities from the full spectrum are then re-scaled by the gamma-detection efficiency and re-seeded into the gamma-gated ToF spectrum for another iteration of this analysis procedure. This procedure allows for the evaluation of low-statistics ToF spectra with significant background fluctuations by testing for agreement with the much higher statistics of the full neutron spectrum. Due to the overall low gamma-detection efficiency, small variations in the size of these neutron peaks will lead to large variations in the predicted intensities of those neutron peaks in the full deconvolution. In the case of peaks such as the peak near 170 ns, which extends into the region where the VANDLE efficiency drops to near zero, comparison with the full neutron spectrum avoids assigning too much feeding intensity to the gamma-gated peak, which would heavily affect the resulting strength distribution calculations. Overall, 4 peaks are fitted to the 1260 keV-gated ToF spectrum (Figure 34). The P_n value for these four peaks combined is 2.6 ± 0.4 %, which shows good agreement with the measurements in (Mazzocchi et al., 2005; Rajabali et al., 2012).

For feedings to the 4+ (2229 keV) state, the same procedure is applied. A ToF spectrum is generated by making an 8 keV gate centered around 969 keV, with a similar gate centered around 939 keV used to normalize the background. The candidate states for the gamma-gated

spectrum are selected from the states observed in the 1260 keV gated spectrum, since the 4+ state de-excites through the 2+ state and so any neutron peaks coincident with the 969 keV gamma ray will also be coincident with the subsequent 1260 keV gamma ray, either of which may be observed. One peak from the 2+ state is also observed, at a similar intensity, from the 4+ state, and is promoted to feeding that level (Figure 35). The apparent peak at 150 ns is not fit because it does not appear lower in the cascade, suggesting that it can be better attributed to a background fluctuation.

Feedings to the second 2+ state (1867 keV) are not fit for two reasons. First, while feeding to this level is expected from the Hauser-Feshbach calculations, none of the candidate peaks seen in the 1260 keV-gated spectrum show good agreement with the 607 keV-gated spectrum (Figure 36). As with the 4+ state, any neutron coincident with the 607 keV gamma ray will also be coincident with the 1260 keV gamma ray. Supporting this, no neutron coincidences are observed in coincidence with the 1867 keV gamma ray that provides the other de-excitation pathway from this state, though the overall low gamma efficiency near 2 MeV means that such non-observation cannot definitively rule out any neutron feedings to this state (Figure 37). Second, the observed 607 keV gamma ray appears in the middle of a set of peaks that are attributable to neutron activation of the Clover detector (see Figures 7 and 32). Such effects have been previously observed to persist even through delayed neutron gating (M. F. Alshudifat et al., 2016), so it is difficult to conclusively assign any n-gamma coincidences here to this 2+ state due to the contamination. It is probable that neutrons are feeding this state, but no neutron peaks can be definitively assigned to populating this state, and so it is excluded from the analysis.

Figures 38 and 39 show the updated neutron spectrum and I_β distribution after including the feedings to the 2+ and 4+ states. The P_n value given by this distribution is 14.0 ± 1.7 %, and the $P_{n\text{-}\gamma}$ is determined to be at least 2.6 ± 0.4%.

5.4 B(GT)

The feeding intensities to each excited state in the beta-decay daughter nucleus are given by a folding of the decay strength with the Fermi intergral. The strength distribution can thus be

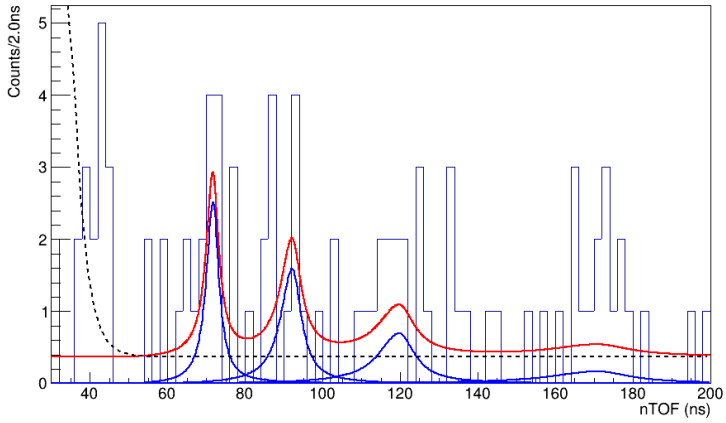

Figure 34: Neutron peaks gated on 1260 keV.

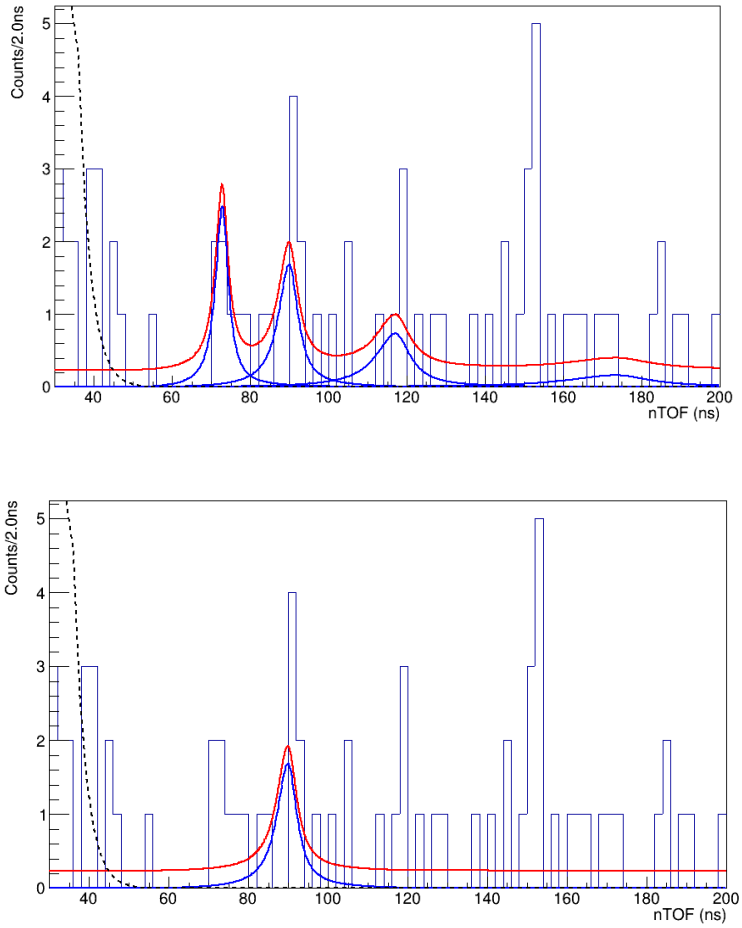

Figure 35: Neutron peaks gated on 969 keV. The upper image shows the candidate peaks from the 1260 keV gated spectrum, and the lower image shows the final peak assignment.

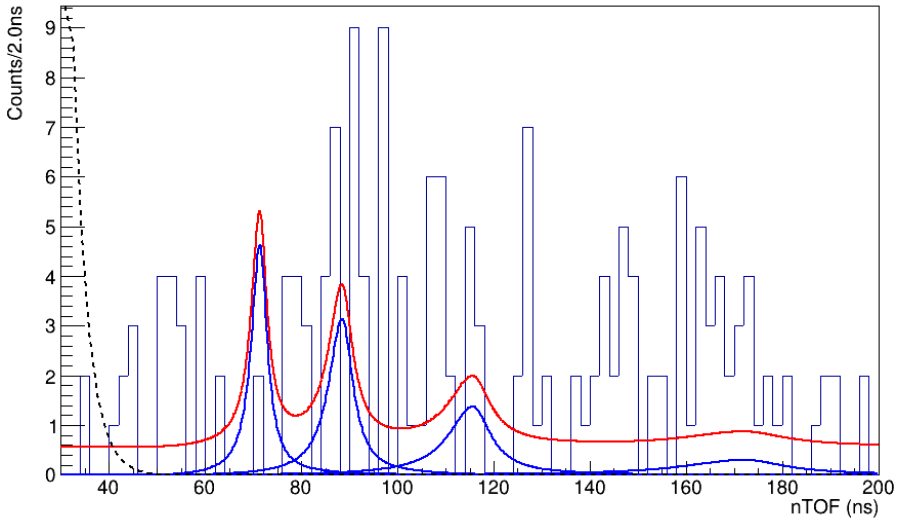

Figure 36: Neutron peak candidates gated on 607 keV. Due to the significant amount of (n,n') background on the Clover, it is difficult to fit any peaks to this spectrum. Any definitive assignments would be highly speculative.

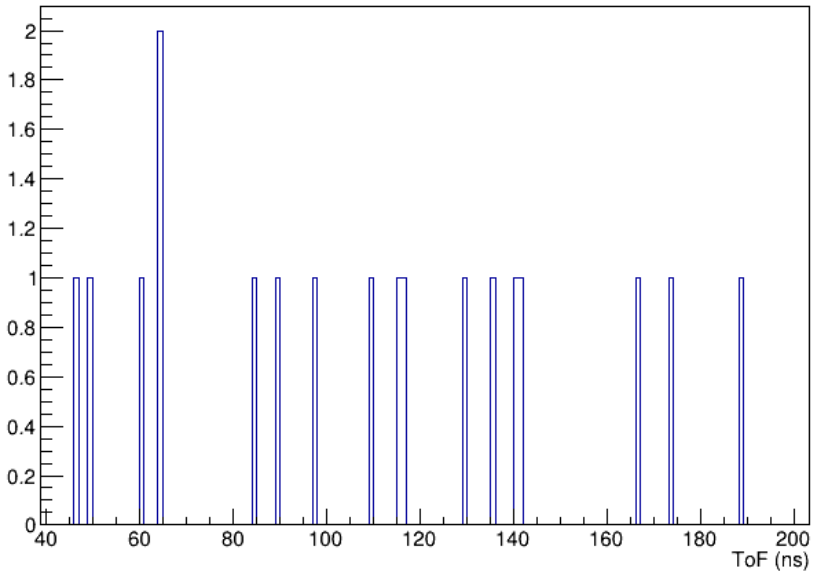

Figure 37: ToF spectrum gated on 1867 keV. The absence of any meaningful counts here makes it difficult to assign any neutrons to the 607 keV gamma ray (Figure 36).

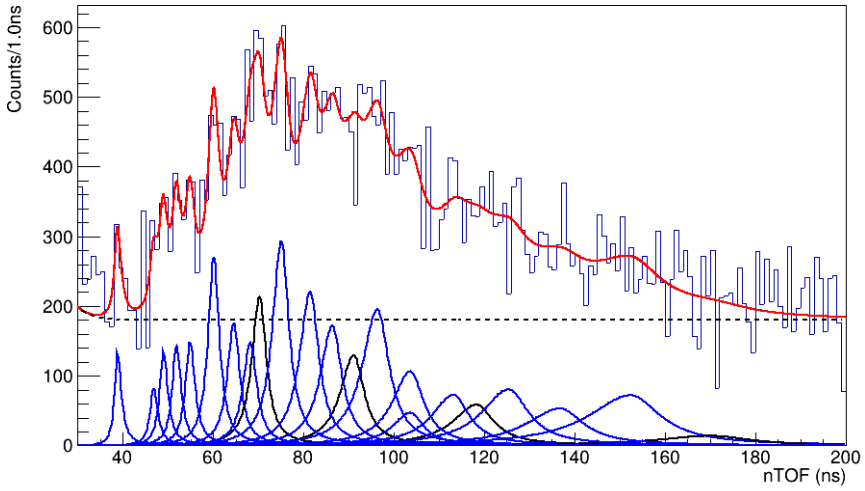

Figure 38: Deconvolution of ^{71}Co neutron spectrum with feedings to excited states. The four peaks feeding the 2+ and 4+ states in ^{70}Ni are colored black, while the peaks feeding the ^{70}Ni ground state are colored blue.

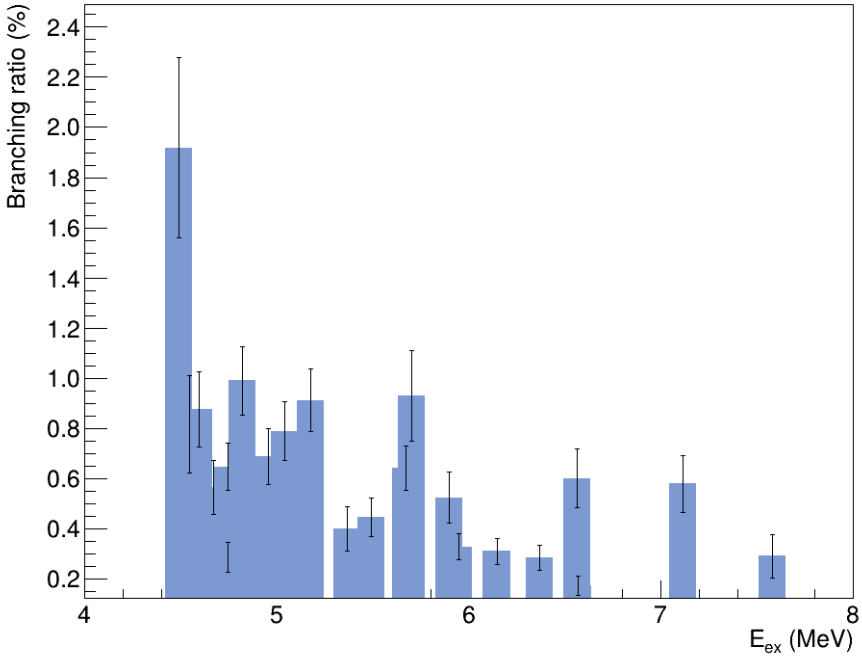

Figure 39: Plot of branching ratio for the full neutron deconvolution. Compared with Figure 29, feeding intensity is spread to higher excitation energies.

obtained from the reciprocal of the partial half-life for each observed state. For states emitting neutrons, the neutron energies and the final excitation energy of the granddaughter nucleus are summed to determine the total excitation energy of the state populated in the daughter nucleus. For states that did not emit neutrons, we relied on data from the Total Absorption Spectroscopy (TAS) measurement of ^{71}Co from (Lyons et al., 2019). TAS uses high-efficiency gamma-ray detection, which makes it well-suited for observing states below S_n that do not emit neutrons, as well as branches from above S_n that de-excite via gamma ray emission instead of delayed neutron emission. The cumulative emission intensities from (Lyons et al., 2019) are re-scaled based on the neutron emission probability measured in this work and unwound to produce absolute branching ratios to each excited state in ^{71}Ni. The full list of energy levels is found in Table 1.

For each of these excited states, a log *ft* value can be calculated and used to construct a value for the B(GT) strength of that state. The B(GT) strength distribution, in terms of $\frac{g_A^2}{4\pi}$ is computed by $B(GT) = K\left(\frac{g_V}{g_A}\right)^2 \frac{1}{ft}$, where K = 6143.6 s (Hardy & Towner, 2009), $\frac{g_A}{g_V}$ = -1.27695 (Zyla, P. A. et. al. (Particle Data Group), 2020), and *ft* is the Fermi integral multiplied by the partial half-life for beta decays to the specific excited state under consideration. The B(GT) distribution that results can be seen in Figure 40. A cumulative B(GT) distribution, combined with the previous data from (Lyons et al., 2019) is shown in Figure 41.

Table 1: List of Energy Levels in ^{71}Ni Fed by Beta Decay

Ex (keV)	Neutron ToF (ns) (± 1.8 ns)	Branching ratio (%)	Branching ratio error (%)	State fed in 70Ni
7582	40.1	0.29	0.09	g.s. (0+)
7115	92.4	0.58	0.11	2229 keV (4+)
6566	48.1	0.17	0.05	g.s. (0+)
6562	71.5	0.6	0.2	1260 keV (2+)
6370	50.3	0.28	0.06	g.s. (0+)
6145	53.2	0.31	0.06	g.s. (0+)
5948	56.2	0.33	0.06	g.s. (0+)
5895	119.6	0.52	0.10	1260 keV (2+)
5704	171.6	0.93	0.18	1260 keV (2+)
5673	61.4	0.64	0.09	g.s. (0+)
5490	65.8	0.45	0.08	g.s. (0+)
5364	69.5	0.40	0.09	g.s. (0+)
5174	76.4	0.91	0.12	g.s. (0+)
5039	82.7	0.79	0.12	g.s. (0+)
4955	87.6	0.69	0.11	g.s. (0+)
4821	97.6	0.99	0.15	g.s. (0+)
4746	104.9	0.93	0.14	g.s. (0+)
4669	114.4	0.57	0.11	g.s. (0+)
4594	126.7	0.88	0.15	g.s. (0+)
4542	138.0	0.82	0.19	g.s. (0+)
4489	153.7	1.9	0.4	g.s. (0+)
4443	--	0.76	0*	--
4243	--	1.7	1.4	--
4052	--	3.0	1.4	--
3843	--	0.8	0*	--
3457	--	3.4	0*	--
3309	--	2.7	1.1	--
3004	--	2.8	0.8	--
2609	--	1.0	1.5	--
2504	--	4.8	1.5	--
2304	--	4.1	1.3	--
2109	--	0.9	0.7	--
1843	--	4.2	1.0	--
1596	--	4.0	1.0	--
1435	--	6.8	1.8	--
1300	--	15	2	--
1074	--	29	2	--
296	--	1.6	0.7	--

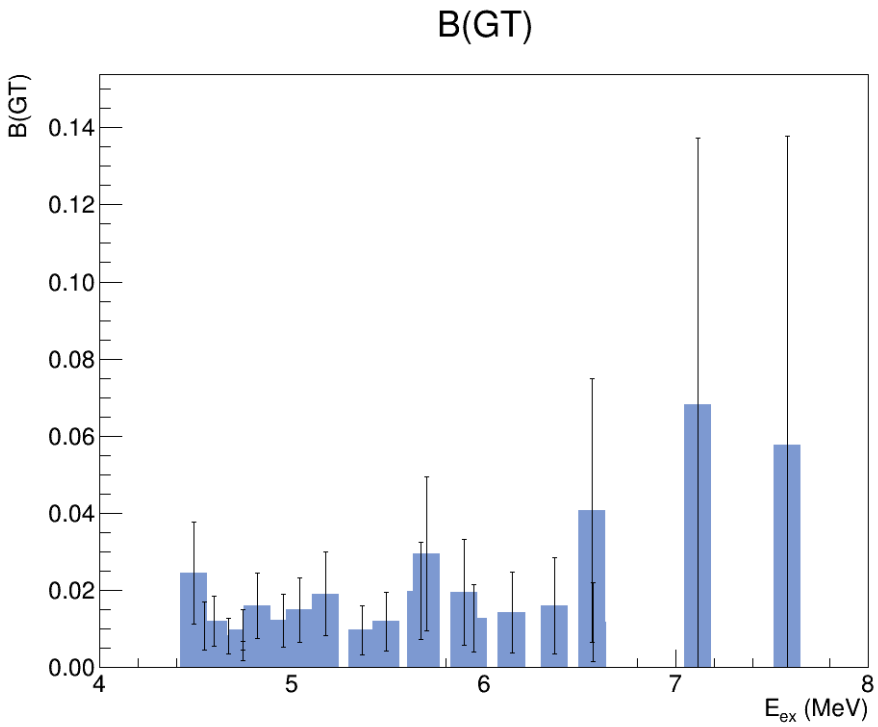

Figure 40: Net B(GT) distribution from the neutron deconvolution in Figures 38 and 39.

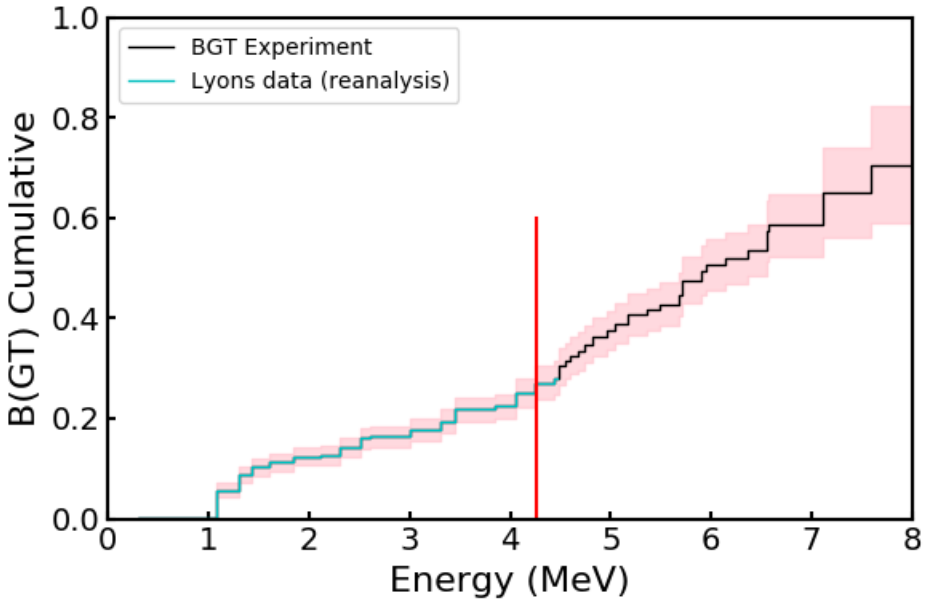

Figure 41: Cumulative B(GT) distribution for ^{71}Co. Black shows the B(GT) for states in this current work, with cyan showing the recomputed B(GT) from the states in Lyons et. al. The red shaded region around the B(GT) represents the cumulative error bars on the B(GT) values. The vertical red line indicates the location of S_n.

Chapter 6: Discussion

6.1 ^{71}Co Decay Past Results

What follows is a summary of the current understanding of ^{71}Co beta decay prior to this work. A decay schematic illustrating these findings is shown in Figure 42. The ^{71}Co decays from a ground state with a 7/2- spin-parity with a half-life of 80 ms. The Q_β value for the decay is 11,040 ± 470 keV (Wang et al., 2021). The low-lying level energy scheme of ^{71}Ni is taken from (Rajabali et al., 2012). The ground state and first excited state have spin-parities of 9/2+ and 7/2+ respectively. Beta decays directly populating these states will be first forbidden transitions due to the required parity change between the mother and daughter nucleus. Higher in energy are a pair of 5/2- states that would be populated via allowed GT decays. These higher-lying states can de-excite via gamma ray emission to either the 9/2+ ground state or to a long-lived 1/2- isomer state at 499 keV.

The neutron separation energy in ^{71}Ni is 4,264 ± 3 keV (Wang et al., 2021), leaving an energy window of 7,066 keV available for beta decays that may result in neutron emission. Allowed GT transitions can populate 5/2-, 7/2- and 9/2- excited states, which, due to the high overall level density are expected to form a continuum of states. Neutron emission from these states may populate either the ground state or one of the excited states in ^{70}Ni.

The main features of the low-lying structure of ^{70}Ni are the spherical states between the 8+ isomer and the 0+ ground state (Sawicka et al., 2004). Of particular note is the 2+ state at 1260 keV. Delayed neutron emission passing through this 2+ state has been observed in several works (Mazzocchi et al., 2005; Rajabali et al., 2012) and the $P_{n\text{-}\gamma}$ branching ratio for this gamma ray was measured at around 3%. Additional 0+ and 2+ states in ^{70}Ni have been observed at 1566 and 1867 keV, respectively (Prokop et al., 2015), and beta-delayed neutron feedings from these states and several more highly excited states have been observed by (Benzoni, 2016). Hauser-Feshbach statistical modeling predicts significant neutron feedings populating the ground state, both 2+ states, and the 4+ state (see Figure 33).

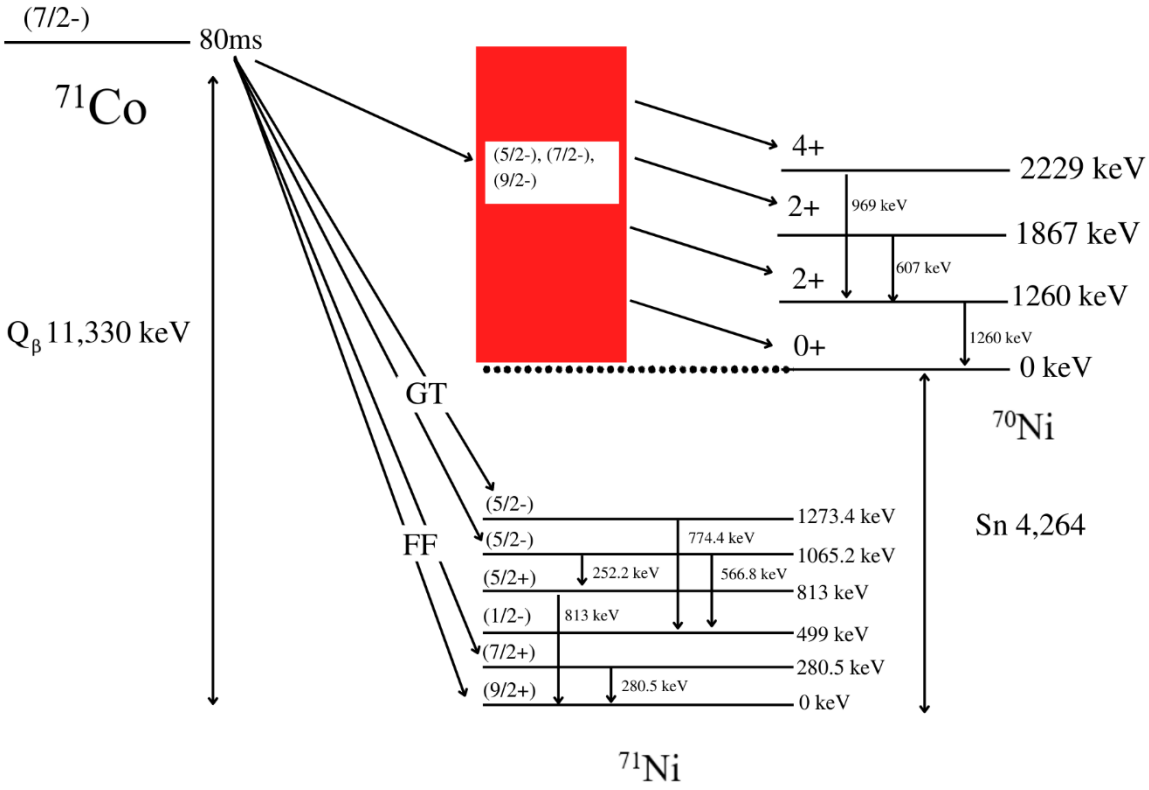

Figure 42: Summary of the current knowledge of the beta decay of ^{71}Co.

6.2 Shell-model interpretation of ^{71}Ni excited states

The shell model framework of 71Co beta decay was discussed by (Rajabali et al., 2012). Neutron-rich cobalt isotopes in the ground state have valence neutrons occupying the $f_{5/2}$ orbital. The highest-energy allowed Gamow-Teller decay transitions will convert one of the $f_{5/2}$ neutrons into an $f_{7/2}$ proton. Decays of g- and p- orbital neutrons directly populating the $f_{7/2}$ orbital are First Forbidden and Second Forbidden transitions, respectively, and will be suppressed in favor of transitions populating the proton g- and p- orbitals above the Z=28 shell gap.

The beta decay strength distribution for the decay of ^{71}Co will thus show two main features: a single low-energy transition corresponding to the $\nu f_{5/2} \rightarrow \pi f_{7/2}$ transition, and a dense continuum of transitions corresponding to the several transitions populating the proton orbitals above the proton shell gap. The energy difference between these features corresponds to the size of the Z=28 shell gap (Figure 43).

Due to the large Q_β value of ^{71}Co and small neutron separation energy in ^{71}Ni for this exotic nucleus, it is expected that a significant portion of the decay strength will extend above S_n. The energy spacing between the low-lying $f_{5/2} \rightarrow f_{7/2}$ transition and the continuum of transitions will indicate the size of the shell gap. This means that TAS data, which can map the strength distribution up to S_n, and neutron spectroscopy, which will map the strength distribution above S_n, will each provide important information in making the shell gap measurement.

^{71}Co has a ground state spin-parity of 7/2-. Allowed GT decays will thus populate spin states 5/2-, 7/2-, and 9/2- in ^{71}Ni. ^{71}Ni has a ground state spin of 9/2+, with a 1/2- isomer state at 499 keV (Rajabali et al., 2012). Allowed beta decays will preferentially populate higher-lying 5/2- states with excitation energies of 1065 and 1273 keV, while the ground state can be populated by first forbidden transitions due to the required parity change. As the density of states rises with increasing excitation energy, additional 5/2-, 7/2-, and 9/2- states will be populated. This occurs via conversion of p- and g- neutrons into protons occupying their respective spin-orbit partner orbitals. Once the excitation energy passes S_n, delayed-neutron emission will become an additional available decay mode, linking the emitter 5/2-, 7/2-, and 9/2- states to the granddaughter 0+, 2+, 4+ and 6+ states, depending on the angular momentum of the emitted neutron. It was suggested that, in the beta decay of ^{70}Co, gamma-ray emission from

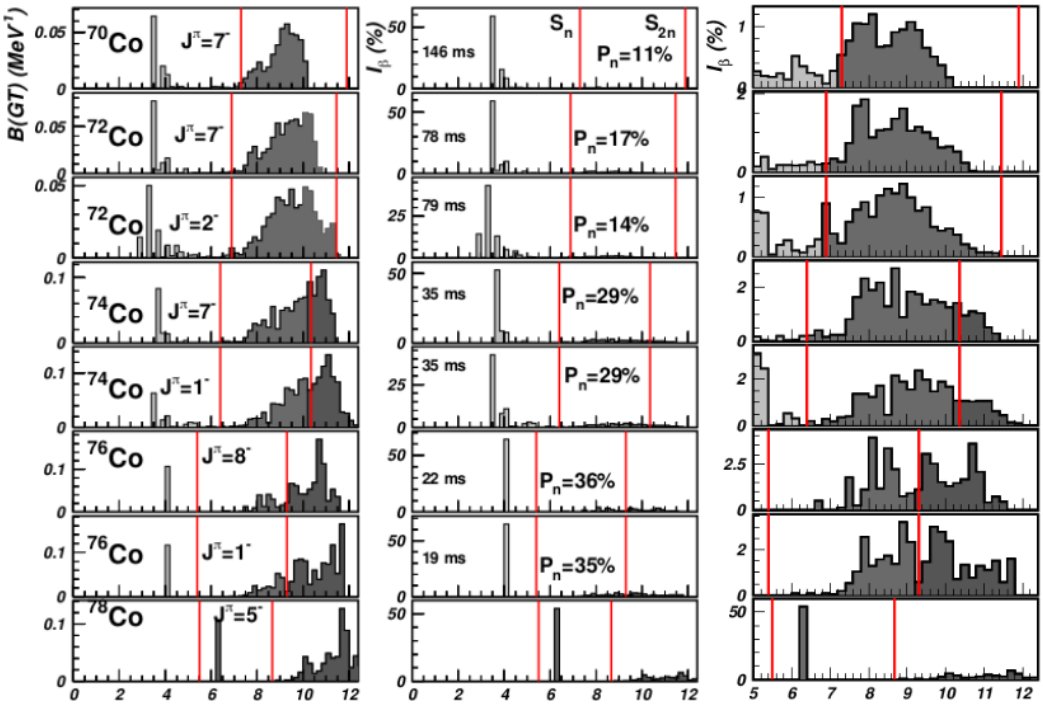

Figure 43: Sample shell model calculations for decays of several cobalt isotopes. Each shows a single strong transition low in energy corresponding to the $f_{5/2} \rightarrow f_{7/2}$ transition, with a continuum of states appearing higher in energy corresponding to transitions of p- and g- orbital neutrons. The energy difference between these sets of transitions gives a measure of the Z=28 shell gap. (Go et al., 2020)

neutron-unbound states in ^{70}Ni would dominate over delayed neutron emission (Spyrou et al., 2016), however, the results from (Lyons et al., 2019) coupled with the significant P_n measurement in this work suggests that the neutron emission mode dominates above S_n in the beta decay of ^{71}Co.

Accurately measuring the P_n value of the decay is also essential for accurately normalizing the decay strength distribution. Estimates of P_n based on gamma spectroscopy are insensitive to neutrons populating the ground state in the granddaughter nucleus, and so will systematically under-estimate the feedings to states above S_n. Due to the effects of the phase space on the observed transition intensities, which scales as $\left(Q_\beta - E_f\right)^5$, small variations in feedings to these neutron-unbound states have large effects on the resulting strength distribution. This is a particular risk in decay studies of odd-even cobalt isotopes, including ^{71}Co, since there is a significant energy window of >1 MeV where delayed neutron emission will not produce any gamma rays. As seen in the results (Table 1), neutron feedings to the ^{70}Ni ground state compete with feedings to gamma-emitting ^{70}Ni states all the way up to 2.3 MeV above S_n, so failure to consider these ground-state-feeding neutrons have the potential to greatly affect the resulting strength distribution.

6.3 Shell Model Calculations

Shell model calculations of the Gamow-Teller strength distribution are performed to help interpret these experimental results. In this work, calculations using two different model spaces are used. The first uses a Hamiltonian with fpgpn interactions, a ^{40}Ca core, and a fully symmetrized valence space consisting of the $\pi 0f_{7/2}$, $\pi 0f_{5/2}$, $\pi 1p_{3/2}$, $\pi 1p_{1/2}$, $\pi 0g_{9/2}$, and $\pi 0g_{7/2}$ orbitals for protons and the $\nu 0f_{7/2}$, $\nu 0f_{5/2}$, $\nu 1p_{3/2}$, $\nu 1p_{1/2}$, $\nu 0g_{9/2}$, and $\nu 0g_{7/2}$ orbitals for neutrons. The second uses a Hamiltonian with Morten Hjorth-Jensen (MHJ) interactions, a ^{48}Ca core, and a reduced, asymmetric valence space of the $\pi 0f_{7/2}$, $\pi f0_{5/2}$, $\pi 1p_{3/2}$, and $\pi 1p_{1/2}$ orbitals for protons and the $\nu 0f_{5/2}$, $\nu 1p_{3/2}$, $\nu 1p_{1/2}$, and $\nu 0g_{9/2}$ orbitals for neutrons. Both model spaces are restricted to considering only one-particle, one-hole excitations, which will be the predominant excitations following decays from a ground state nucleus. This truncation of the model space is used to

make the calculations tractable, as the computational complexity increases dramatically as the configuration space of the nucleons expands. In both models, the relative excitation energies of the orbitals are adjusted to fit the data. Close fits to the data can be seen in Figures 44 and 45, and a summary of the respective orbital energy levels used in the calculations can be found in Table 2. These orbital energies listed in Table 2 represent energies used to initialize the shell model calculations. The resulting energy levels of the orbitals are modified from these initial values as nucleons are added to the orbitals as the result of residual interactions.

The MHJ reflect the expected features of the shell structure impact on the decay to ^{71}Ni. The valence space includes only the orbitals expected to play the largest role in the decay process and posits a sizable Z=28 shell gap between the $f_{5/2}\rightarrow f_{7/2}$ transitions and the higher-energy p- and g- orbital transitions, as seen in Figure 44. However, the data found in Lyons and this work seems at odds with this treatment. The strength distribution shows a much more heavily fragmented $f_{5/2}\rightarrow f_{7/2}$ transition than the MHJ model predicts, with a steadily accumulating strength up to the S_n. This work shows that accumulation continue above S_n, with little evidence of the significant increase in strength associated with the continuum states across the Z=28 shell gap.

The fpgpn model, by contrast, expands the valence space to also include the spin-orbit partner orbitals $\pi g_{9/2}$, $\pi g_{7/2}$, $\nu 0f_{7/2}$, and $\nu 0g_{7/2}$. The best-fitting fpgpn model also makes use of a significantly reduced shell gap, so that the continuum states set in well below S_n, and so is able to more accurately model the fragmentation of the low-lying transitions and the steady accumulation of strength across S_n observed in the data (Figure 45). The shell gap is observed to be approximately 2 MeV, with the continuum of excited states appearing at about 3 MeV in excitation energy. This particular fpgpn model has previously been used to model the decay strength of other neutron-rich nickel isotopes (Go et al., 2020; Spyrou et al., 2016), suggesting that it is accurately capturing some of the important structure effects in this region of the nuclear chart.

This model showing a shell gap of 2 MeV for ^{71}Ni is at odds with the predicted shell gap of 5 MeV that is expected from ^{78}Ni (Grawe et al., 2007). This is due to the need to initialize the $\pi 0f_{7/2}$ orbital at –4.955 MeV to match the experimental data here. Raising the $f_{7/2}$ orbital in this way initializes it above both of the p orbitals, obliterating any expectation of a shell gap at Z=28.

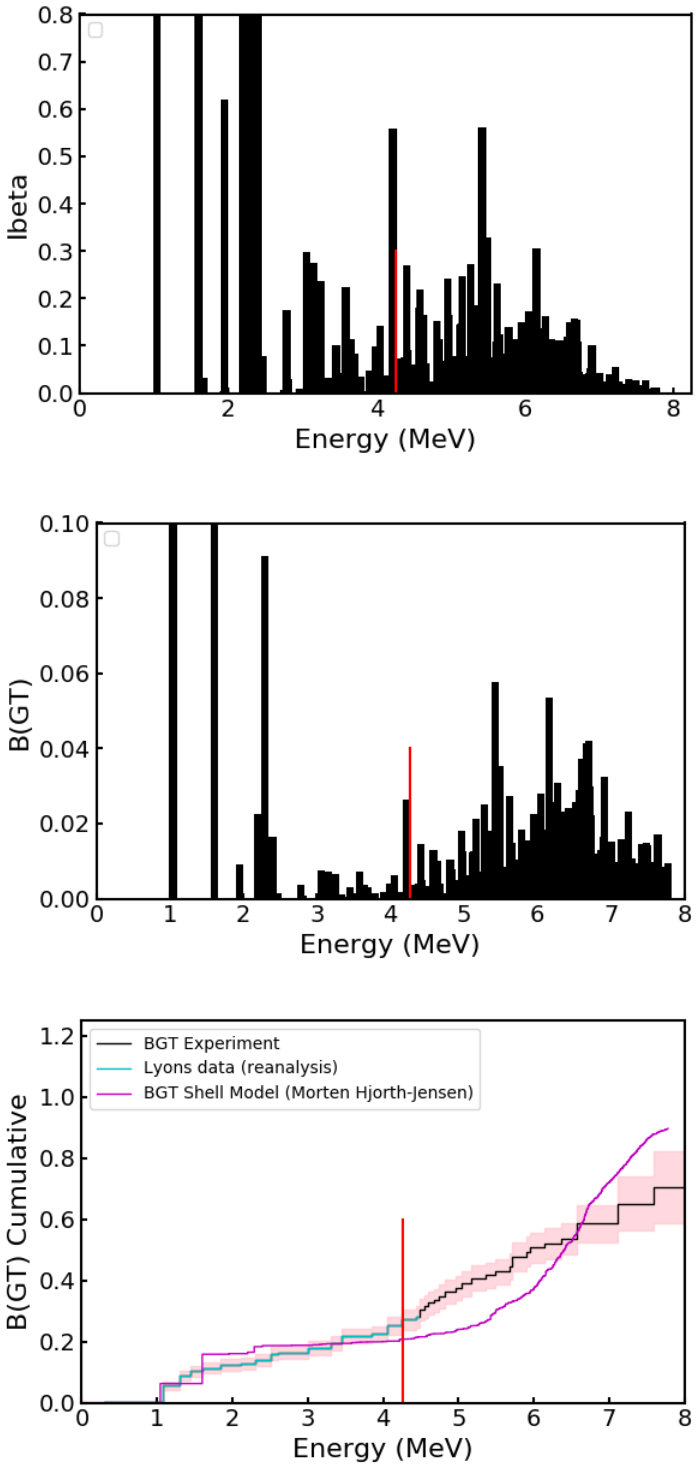

Figure 44: Results of best-fitting MHJ shell model calculations. The top image shows the plot of the branching ratios, middle shows the resulting B(GT) distribution, and the bottom image shows the cumulative B(GT) compared with the experimental data. This model differs markedly from the data, modeling a significant gap between the low-lying transitions and the steady rise due to the continuum states, while the data shows a steady rise through the entire distribution.

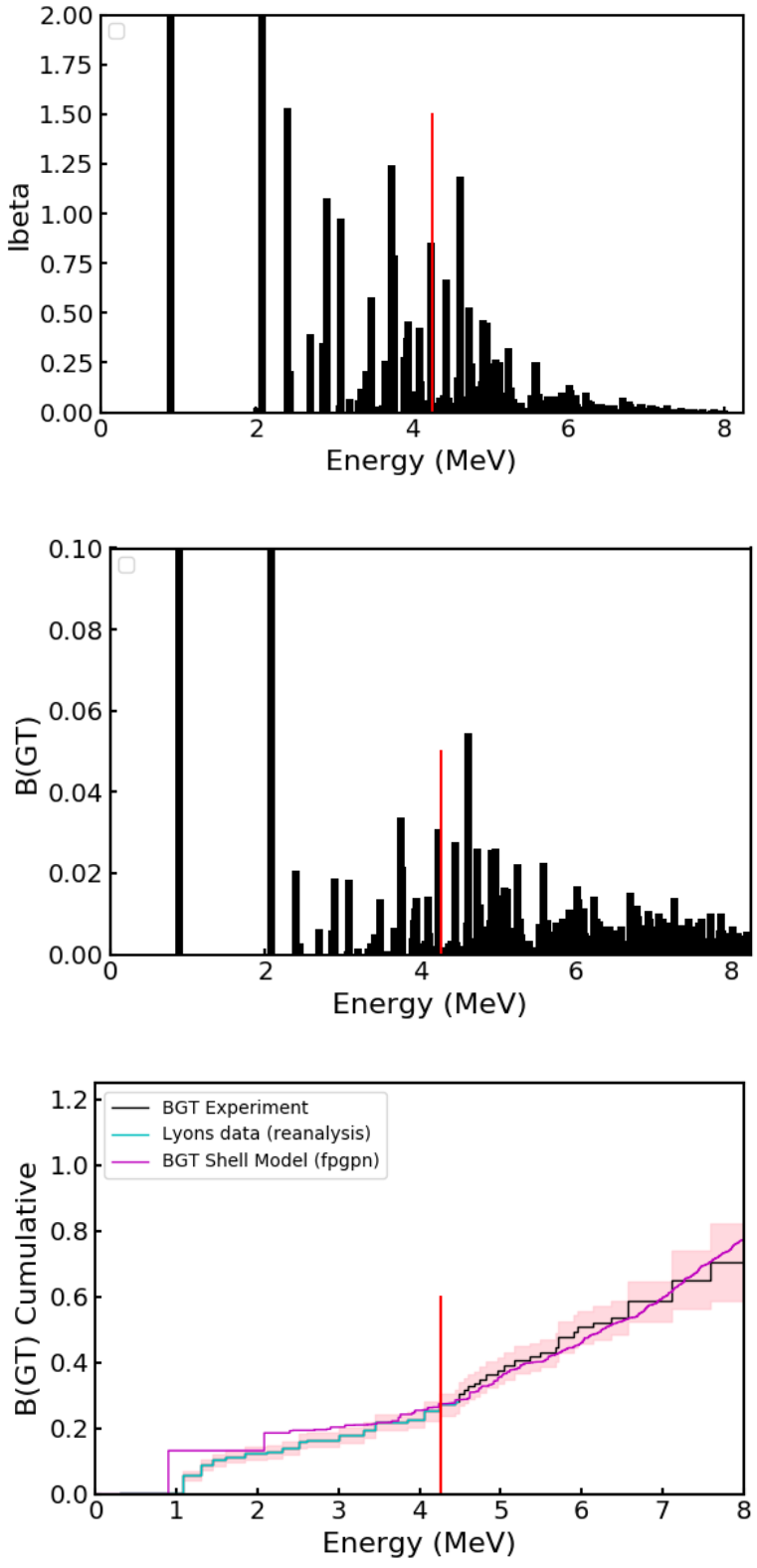

Figure 45: Results of best-fitting fpgpn shell model calculations. The top image shows the plot of the branching ratios, middle shows the resulting B(GT) distribution, and the bottom image shows the cumulative B(GT) compared with the experimental data. This model shows good overall agreement with the data.

Table 2: List of orbital energies used for shell model calculations.

	fpgpn	M H-J
π0f7/2	-4.955	-20.06
π1p3/2	-6.044	-14.94
π0f5/2	-1.683	-13.44
π1p1/2	-5.544	-12.04
π0g9/2	0	–
π0g7/2	6.0	–
ν0f7/2	-4.624	–
ν1p3/2	-2.679	-8.39
ν0f5/2	2.617	-8.54
ν1p1/2	-1.137	-7.21
ν0g9/2	3.4	-5.86
ν0g7/2	8.9	–

While a small shell gap does nevertheless emerge from the calculations, it is sharply reduced compared to the expected 5 MeV expected in ^{78}Ni. Initializing the $\pi f_{7/2}$ orbital at -8.955 MeV, 4 MeV lower than what is needed to match the data, reproduces the expected shell gap of about 5 MeV, giving a clear contrast between the expected behavior predicted based on ^{78}Ni and the model that best reproduces the experimental data (Figure 46).

6.4 Single-proton excitations in neutron-rich Cobalt Isotopes

In order to explore how the placement of the $f_{7/2}$ proton orbital will be reflected in the structure of neutron-rich cobalt isotopes, systematic shell-model calculations were performed for the series of isotopes with 40<N<50 with fpgpn interactions and with three sets of single-particle energies. The ^{71}Co ground state has a spin-parity of 7/2- owing to the unpaired proton in the $f_{7/2}$ orbital and the full pairing of neutrons. Low-lying one-proton excitations of ^{71}Co will be generated with the unpaired $f_{7/2}$ proton being scattered into into the $f_{5/2}$, $p_{3/2}$, or $p_{1/2}$ orbitals, creating states with spin-parities of 5/2-, 3/2-, and 1/2- respectively. The excitation energies of these one-proton excitations are thus expected to show a dependence of the size of the Z=28 shell gap.

The effect of a clearly defined shell gap can be seen from modeling these one-proton excitations in ^{77}Co. ^{78}Ni has been shown to be a good doubly-magic nucleus (Taniuchi et al., 2019), so the proton excitations in ^{77}Co excite the proton across the clearly-defined Z=28 shell gap. Additionally, the closed N=50 neutron shell means that no fragmentation of the excited states will occur based on different occupancies of neutron orbitals; the excitation spectrum will be pure proton excitations in ^{77}Co.

The effects of the proton single-particle energies on the excitation energies for ^{77}Co and ^{71}Co are shown in Figures 47 and 48, respectively. These calculations are performed using the NuShellX shell model code and make use of the fpgpn interaction. In ^{77}Co, there is a direct, linear dependence of the proton excitations on the placement of the $\pi f_{7/2}$ orbital. This observation indicates a clear shell gap effect for two reasons. The energy of the excited states increases as the energy gap between the $f_{7/2}$ orbital and the other orbitals is lowered, which is indicative of the

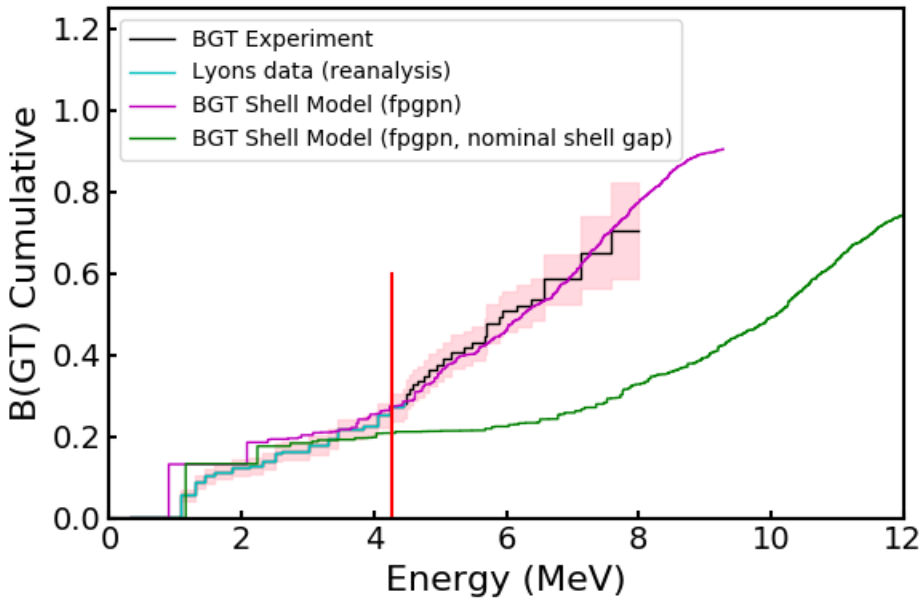

Figure 46: B(GT) comparison of fpgpn models with varied shell gap initializations. Magenta shows the initialization with the best fit, which is consistent with the models used in (Spyrou et al., 2016) *and* (Go et al., 2020). *This initialization places the $f_{7/2}$ proton orbital above the p-orbitals, so the shell gap that emerges is significantly reduced. Green shows the result of initializing the $f_{7/2}$ orbital in a manner consistent with the expectations from ^{78}Ni, with a resulting 5 MeV shell gap that is consistent with those expectations.*

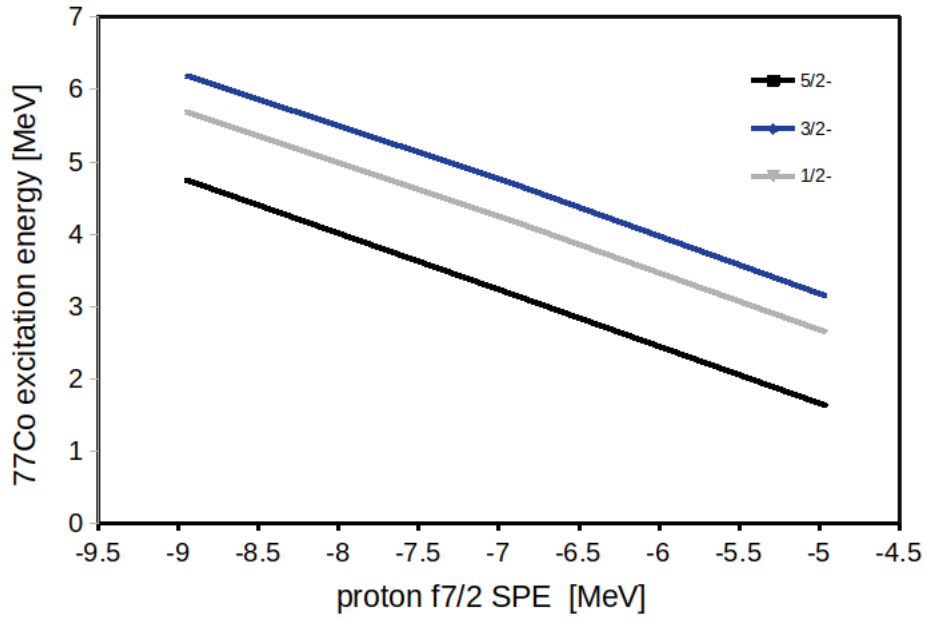

Figure 47: Low-lying single-proton excitations in ^{77}Co. Promoting an $f_{7/2}$ proton across the shell gap to an $f_{5/2}$, $p_{3/2}$, or $p_{1/2}$ orbital gives excitation spin-parities of 5/2-, 3/2-, and 1/2-, respectively. These states show a linear dependence between their excitation energies and the energy initialization of the $f_{7/2}$ orbital, indicating clear "core-valence" independence between these orbitals. This behavior is a characteristic of the magic numbers.

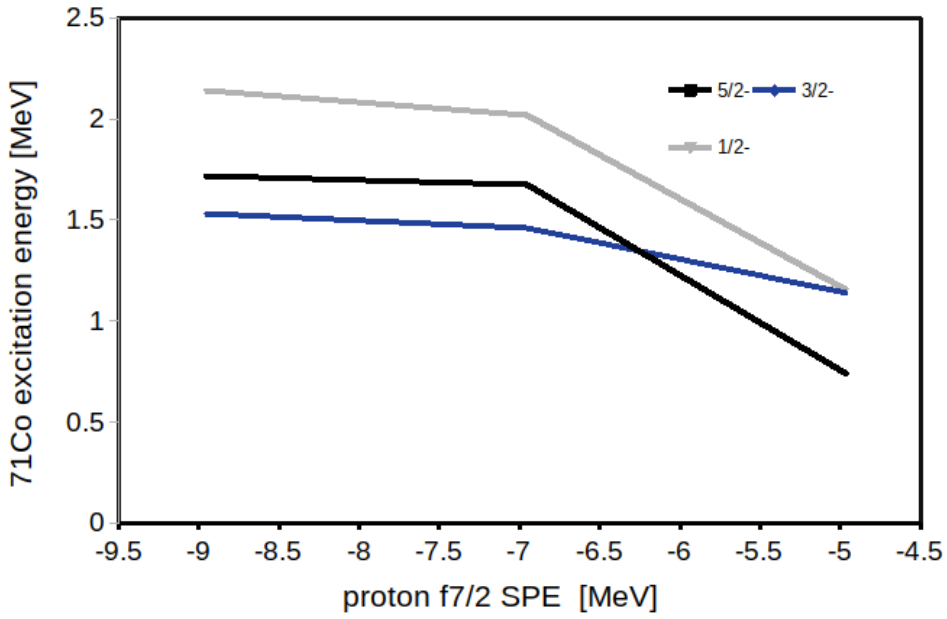

Figure 48: Low-lying single-proton excitations in ^{71}Co. Unlike in Figure 47, the excitation energies of the single-proton states show clear evidence of cross-shell correlations, with the excited states being pulled down by the lowering of the $f_{7/2}$ orbital. The cross-shell correlations between the proton orbitals are indicative of the melting of the Z=28 shell in this region. Proton excitations are not a good probe of the size of the shell gap here, while the strength distribution is. Compare the trend in the predicted shell gap here with that in Figure 46.

size of the shell gap increasing as the placement of the $f_{7/2}$ orbital is lowered. The trend shows a clear independence between the initial placement of the $f_{7/2}$ orbital and the eventual placements of the $f_{5/2}$ and p orbitals, which is indicative of a clear, well-defined gap between the $f_{7/2}$ orbital and the $f_{5/2}$ and p orbitals.

In contrast, the one-proton excitations in ^{71}Co shows a significant deviation from the simple linear dependence seen in ^{77}Co. This is due to the effects of configuration mixing, which will become more prominent with decreasing shell gap. In ^{71}Co, the gap between the ground state and the excited states are fairly insensitive to the placement of the $f_{7/2}$ orbital. This change is a clear indication of significant cross-shell correlations in this isotope, which would be consistent with the breakdown of the Z=28 shell gap in this region.

Additionally, the insensitivity of the proton excitation energies to the placement of the $f_{7/2}$ orbital suggests that the energies of excited states in ^{71}Ni are not easily related to the proton shell gap. In contrast, we have shown clearly that the strength distribution remains sensitive to the shell gap (Figure 46) in the decay of ^{71}Co. This suggests that the measured strength distribution is a reliable probe of the shell gap under these conditions, as it retains its sensitivity to the shell gap even in regions where single-particle excitations no longer reflect sensitivity to this observable. Full decay studies, including both TAS and neutron spectroscopy, thus provide an essential and irreplaceable means of measuring magic nuclei in these neutron-rich settings.

Bibliography

Alshudifat, M. F., Grzywacz, R., Madurga, M., Gross, C. J., Rykaczewski, K. P., Batchelder, J. C., Bingham, C., Borzov, I. N., Brewer, N. T., Cartegni, L., Fijałkowska, A., Hamilton, J. H., Hwang, J. K., Ilyushkin, S. V., Jost, C., Karny, M., Korgul, A., Królas, W., Liu, S. H., … Zganjar, E. F. (2016). Reexamining Gamow-Teller decays nearNi78. In *Physical Review C* (Vol. 93, Issue 4). https://doi.org/10.1103/physrevc.93.044325

Alshudifat, M., Grzywacz, R., & Paulauskas, S. V. (2015). Development of a Segmented Scintillator for Decay Studies. In *Physics Procedia* (Vol. 66, pp. 445–450). https://doi.org/10.1016/j.phpro.2015.05.056

Benzoni, G. (2016). *Investigation of 70, 72, 74 Ni From Beta Decay of 70, 72,74 Co*. Nuclear Structure, Knoxville, Tennessee.

Burbidge, E. M., Burbidge, G. R., Fowler, W. A., & Hoyle, F. (1957). Synthesis of the elements in stars. *Reviews of Modern Physics*, *29*(4), 547–650.

Caurier, E. (2004). *Shell Model Code ANTOINE*.

Daugas, J. M., Grzywacz, R., Lewitowicz, M., Achouri, L., Angélique, J. C., Baiborodin, D., Bennaceur, K., Bentida, R., Béraud, R., Borcea, C., Bingham, C., Catford, W. N., Emsallem, A., de France, G., Grawe, H., Jones, K. L., Lemmon, R. C., Lopez Jimenez, M. J., Nowacki, F., … Stanoiu, M. (2000). The 8 isomer in 78Zn and the doubly magic character of 78Ni. In *Physics Letters B* (Vol. 476, Issues 3–4, pp. 213–218). https://doi.org/10.1016/s0370-2693(00)00177-5

Erler, J., Birge, N., Kortelainen, M., Nazarewicz, W., Olsen, E., Perhac, A. M., & Stoitsov, M. (2012). The limits of the nuclear landscape. *Nature*, *486*(7404), 509–512.

Go, S., Grzywacz, R., Mazzocchi, C., Liddick, S. N., Alshudifat, M., Batchelder, J. C., Baumann, T., Ciemny, A. A., Ginter, T. N., Gross, C. J., Kolos, K., Korgul, A., Paulauskas, S. V., Prokop, C. J., Rajabali, M. M., Rykaczewski, K. P., Taylor, S., & Xiao, Y. (2020). Mapping of fragmented νf5/2→πf7/2 transitions in the Co73→Ni73 decay. *Physical Review. C*, *102*(4). https://doi.org/10.1103/physrevc.102.044331

Grawe, H., Langanke, K., & Martínez-Pinedo, G. (2007). Nuclear structure and astrophysics. *Reports on Progress in Physics. Physical Society (Great Britain)*, *70*(9), 1525–1582.

Hardy, J. C., & Towner, I. S. (2009). Superallowed0 →0 nuclearβdecays: A new survey with precision tests of the conserved vector current hypothesis and the standard model. In *Physical Review C* (Vol. 79, Issue 5). https://doi.org/10.1103/physrevc.79.055502

Hjorth-Jensen, M., Kuo, T. T. S., & Osnes, E. (1995). Realistic effective interactions for nuclear systems. *Physics Reports*, *261*(3–4), 125–270.

Huck, A., Klotz, G., Knipper, A., Miehé, C., Richard-Serre, C., Walter, G., Poves, A., Ravn, H. L., & Marguier, G. (1985). Beta decay of the new isotopes 52K, 52Ca, and 52Sc; a test of the shell model far from stability. *Physical Review C: Nuclear Physics*, *31*(6), 2226–2237.

Krane, K. S., & Lynch, W. G. (1989). Introductory Nuclear Physics. In *Physics Today* (Vol. 42, Issue 1, pp. 78–78). https://doi.org/10.1063/1.2810884

Lisetskiy, A. F., Brown, B. A., Horoi, M., & Grawe, H. (2004). New T=1 effective interactions for the f5/2 p3/2 p1/2 g9/2 model space; Implications for valence-mirror symmetry and seniority isomers. In *arXiv [nucl-th]*. arXiv. http://arxiv.org/abs/nucl-th/0402082

Lyons, S., Spyrou, A., Liddick, S. N., Naqvi, F., Crider, B. P., Dombos, A. C., Bleuel, D. L., Brown, B. A., Couture, A., Crespo Campo, L., Engel, J., Guttormsen, M., Larsen, A. C.,

Lewis, R., Möller, P., Mosby, S., Mumpower, M. R., Ney, E. M., Palmisano, A., … Quinn, S. J. (2019). Co69,71 β -decay strength distributions from total absorption spectroscopy. In *Physical Review C* (Vol. 100, Issue 2). https://doi.org/10.1103/physrevc.100.025806

Madurga, M., Surman, R., Borzov, I. N., Grzywacz, R., Rykaczewski, K. P., Gross, C. J., Miller, D., Stracener, D. W., Batchelder, J. C., Brewer, N. T., Cartegni, L., Hamilton, J. H., Hwang, J. K., Liu, S. H., Ilyushkin, S. V., Jost, C., Karny, M., Korgul, A., Królas, W., … Zganjar, E. F. (2012). New half-lives of r-process Zn and Ga isotopes measured with electromagnetic separation. *Physical Review Letters*, *109*(11), 112501.

Matei, C., Bardayan, D. W., Blackmon, J. C., Cizewski, J. A., Grzywacz, R. K., Liddick, S. N., Padgett, S. W., Peters, W. A., Sarazin, F., McDaniel, F. D., & Doyle, B. L. (2009). Development of a Versatile Array of Neutron Detectors at Low Energy. In *AIP Conference Proceedings*. https://doi.org/10.1063/1.3120156

Mayer, M. G. (1949). On closed shells in nuclei. II. *The Physical Review*, *75*(12), 1969–1970.

Mazzocchi, C., Grzywacz, R., Batchelder, J. C., Bingham, C. R., Fong, D., Hamilton, J. H., Hwang, J. K., Karny, M., Krolas, W., Liddick, S. N., Lisetskiy, A. F., Morton, A. C., Mantica, P. F., Mueller, W. F., Rykaczewski, K. P., Steiner, M., Stolz, A., & Winger, J. A. (2005). Low energy structure of even–even Ni isotopes close to 78Ni. In *Physics Letters B* (Vol. 622, Issues 1–2, pp. 45–54). https://doi.org/10.1016/j.physletb.2005.07.006

Mazzocchi, C., Grzywacz, R., Batchelder, J. C., Bingham, C. R., Fong, D., Hamilton, J. H., Hwang, J. K., Karny, M., Królas, W., Liddick, S. N., Morton, A. C., Mantica, P. F., Mueller, W. F., Rykaczewski, K. P., Steiner, M., Stolz, A., & Winger, J. A. (n.d.). Beta-

delayed γ and neutron emission near the double shell closure at 78Ni. In *The 4th International Conference on Exotic Nuclei and Atomic Masses* (pp. 93–94). https://doi.org/10.1007/3-540-37642-9_26

Mazzocchi, C., Rykaczewski, K. P., Korgul, A., Grzywacz, R., Bączyk, P., Bingham, C., Brewer, N. T., Gross, C. J., Jost, C., Karny, M., Madurga, M., Mendez, A. J., Miernik, K., Miller, D., Padgett, S., Paulauskas, S. V., Stracener, D. W., Wolińska-Cichocka, M., & Borzov, I. N. (2013). New half-life measurements of the most neutron-rich arsenic and germanium isotopes. In *Physical Review C* (Vol. 87, Issue 3). https://doi.org/10.1103/physrevc.87.034315

Morales, A. I., & et al. (2016). Low-Lying Excitations in 72Ni. *Physical Review C: Nuclear Physics*.

Mumpower, M. R., Surman, R., McLaughlin, G. C., & Aprahamian, A. (2016). The impact of individual nuclear properties onr-process nucleosynthesis. *Progress in Particle and Nuclear Physics*, *86*, 86–126.

Okumura, S., Kawano, T., Jaffke, P., Talou, P., & Chiba, S. (2018). 235U(n, f) Independent fission product yield and isomeric ratio calculated with the statistical Hauser–Feshbach theory. *Journal of Nuclear Science and Technology*, *55*(9), 1009–1023.

Paulauskas, S. V. (2013). *Beta-Delayed Neutron Spectroscopy of Fission Fragments Using the Versatile Array of Neutron Detectors at Low Energy*. University of Tennessee.

Paulauskas, S. V., Madurga, M., Grzywacz, R., Miller, D., Padgett, S., & Tan, H. (2014). A digital data acquisition framework for the Versatile Array of Neutron Detectors at Low Energy (VANDLE). In *Nuclear Instruments and Methods in Physics Research Section A:*

Accelerators, Spectrometers, Detectors and Associated Equipment (Vol. 737, pp. 22–28). https://doi.org/10.1016/j.nima.2013.11.028

Peters, W. A., Ilyushkin, S., Madurga, M., Matei, C., Paulauskas, S. V., Grzywacz, R. K., Bardayan, D. W., Brune, C. R., Allen, J., Allen, J. M., Bergstrom, Z., Blackmon, J., Brewer, N. T., Cizewski, J. A., Copp, P., Howard, M. E., Ikeyama, R., Kozub, R. L., Manning, B., … Walter, D. (2016). Performance of the Versatile Array of Neutron Detectors at Low Energy (VANDLE). In *Nuclear Instruments and Methods in Physics Research Section A: Accelerators, Spectrometers, Detectors and Associated Equipment* (Vol. 836, pp. 122–133). https://doi.org/10.1016/j.nima.2016.08.054

Prokop, C. J., Crider, B. P., Liddick, S. N., Ayangeakaa, A. D., Carpenter, M. P., Carroll, J. J., Chen, J., Chiara, C. J., David, H. M., Dombos, A. C., Go, S., Harker, J., Janssens, R. V. F., Larson, N., Lauritsen, T., Lewis, R., Quinn, S. J., Recchia, F., Seweryniak, D., … Zhu, S. (2015). New low-energy0+state and shape coexistence inNi70. *Physical Review C: Nuclear Physics*, *92*(6). https://doi.org/10.1103/physrevc.92.061302

Rae, W. D. M. (2008). *NuShellX*.

Rajabali, M. M., Grzywacz, R., Liddick, S. N., Mazzocchi, C., Batchelder, J. C., Baumann, T., Bingham, C. R., Darby, I. G., Ginter, T. N., Ilyushkin, S. V., Karny, M., Królas, W., Mantica, P. F., Miernik, K., Pfützner, M., Rykaczewski, K. P., Weisshaar, D., & Winger, J. A. (2012). β decay of 71,73Co: Probing single-particle states approaching doubly magic 78Ni. In *Physical Review C* (Vol. 85, Issue 3). https://doi.org/10.1103/physrevc.85.034326

Roberts, R. B., Hafstad, L. R., Meyer, R. C., & Wang, P. (1939). The delayed neutron emission which accompanies fission of uranium and thorium. *The Physical Review*, *55*(7), 664–664.

Sawicka, M., Matea, I., Grawe, H., Grzywacz, R., Pfützner, M., Lewitowicz, M., Daugas, J. M., Brown, B. A., Lisetskiy, A., Becker, F., Bélier, G., Bingham, C., Borcea, R., Bouchez, E., Buta, A., Dragulescu, E., de France, G., Georgiev, G., Giovinazzo, J., … Żylicz, J. (2004). Beta-decay of 71Co and 73Co. In *The European Physical Journal A* (Vol. 22, Issue 3, pp. 455–459). https://doi.org/10.1140/epja/i2004-10047-3

Shimizu, N. (2013). *Nuclear Shell-Model Code for Massive Parallel Computation, KSHELL*.

Söderström, P.-A., & et al. (2015). Two-hole structure beyond 78Ni: Existence of a μs isomer of 76Co and beta decay into 76Ni. *Physical Review C: Nuclear Physics*.

Sonzogni, A. (2007). NNDC Chart of Nuclides. In *ND2007*. https://doi.org/10.1051/ndata:07530

Spyrou, A., Liddick, S. N., Naqvi, F., Crider, B. P., Dombos, A. C., Bleuel, D. L., Brown, B. A., Couture, A., Crespo Campo, L., Guttormsen, M., Larsen, A. C., Lewis, R., Möller, P., Mosby, S., Mumpower, M. R., Perdikakis, G., Prokop, C. J., Renstrøm, T., Siem, S., … Valenta, S. (2016). Strong Neutron-γ Competition above the Neutron Threshold in the Decay of ^{70}Co. *Physical Review Letters*, *117*(14), 142701.

Talmi, I. (1993). *Simple models of complex nuclei*. Harwood-Academic.

Taniuchi, R., Santamaria, C., Doornenbal, P., Obertelli, A., Yoneda, K., Authelet, G., Baba, H., Calvet, D., Château, F., Corsi, A., Delbart, A., Gheller, J.-M., Gillibert, A., Holt, J. D., Isobe, T., Lapoux, V., Matsushita, M., Menéndez, J., Momiyama, S., … Xu, Z. Y. (2019). 78Ni revealed as a doubly magic stronghold against nuclear deformation. *Nature*, *569*(7754), 53–58.

Taylor, S. (2018). *Beta-Delayed Neutron Spectroscopy of 135-136Sb Using the Versatile Array of Neutron Detectors at Low Energy (VANDLE)* [PhD Thesis]. University of Tennessee.

Thornsberry, C. (2018). *Proton Transfer Reactions Studied Using the Versatile Array of Neutron Detectors at Low Energy (VANDLE)* [PhD Thesis]. University of Tennessee.

Van Isacker, P. (2011). Partial conservation of seniority in nuclei. *International Journal of Modern Physics E*, *20*(02), 191–198.

Wang, M., Huang, W. J., Kondev, F. G., Audi, G., & Naimi, S. (2021). The AME 2020 atomic mass evaluation (II). Tables, graphs and references. *Chinese Physics C*, *45*(3), 030003.

Wienholtz, F., Beck, D., Blaum, K., Borgmann, C., Breitenfeldt, M., Cakirli, R. B., George, S., Herfurth, F., Holt, J. D., Kowalska, M., Kreim, S., Lunney, D., Manea, V., Menéndez, J., Neidherr, D., Rosenbusch, M., Schweikhard, L., Schwenk, A., Simonis, J., … Zuber, K. (2013). Masses of exotic calcium isotopes pin down nuclear forces. *Nature*, *498*(7454), 346–349.

Xiao, Y., Go, S., Grzywacz, R., Orlandi, R., Andreyev, A. N., Asai, M., Bentley, M. A., de Angelis, G., Gross, C. J., Hausladen, P., Hirose, K., Hofmann, S., Ikezoe, H., Jenkins, D. G., Kindler, B., Léguillon, R., Lommel, B., Makii, H., Mazzocchi, C., … Wadsworth, R. (2019). Search for α decay of Te104 with a novel recoil-decay scintillation detector. In *Physical Review C* (Vol. 100, Issue 3). https://doi.org/10.1103/physrevc.100.034315

Zyla, P. A. et. al. (Particle Data Group). (2020). Review of Particle Physics. *Prog. Theor. Exp. Phys.*, *2020*(8).

Vita

Originally from Massachusetts, Andrew M. Keeler grew up in Needham, Massachusetts. After high school, he attended Wheaton College (Illinois) and received a Bachelor of Science degree in Physics and the Philosophy of Science. While at Wheaton, he worked with Dr. Heather Whitney in the field of medical physics as her assistant.

After taking a year off between undergraduate and graduate schools, Andrew chose to attend the University of Tennessee, Knoxville to pursue a Doctor of Physics degree, concentrating in nuclear physics. After graduation, Andrew plans to apply for a medical physics certificate program, followed by a medical physics residency. He currently resides with his wife in Chicago, Illinois. He is incredibly grateful for all the support from his wife, advisor, and family as he begins his next journey.